Massive Multi-Antenna Communications with Low-Resolution Data Converters

SVEN JACOBSSON

CHALMERS

UNIVERSITY OF TECHNOLOGY

Communications, Antennas, and Optical Networks
Department of Electrical Engineering
Chalmers University of Technology
Gothenburg, Sweden, 2019

Massive Multi-Antenna Communications with Low-Resolution Data Converters

This thesis has been prepared using LaTeX and Ti*k*Z.

Abstract

Massive multi-user (MU) multiple-input multiple-output (MIMO) will be a core technology in future cellular communication systems. In massive MU-MIMO systems, the number of antennas at the base station (BS) is scaled up by several orders of magnitude compared to traditional multi-antenna systems with the goals of enabling large gains in capacity and energy efficiency. However, scaling up the number of active antenna elements at the BS will lead to significant increases in power consumption and system costs unless power-efficient and low-cost hardware components are used. In this thesis, we investigate the performance of massive MU-MIMO systems for the case when the BS is equipped with low-resolution data converters.

First, we consider the massive MU-MIMO uplink for the case when the BS uses low-resolution analog-to-digital converters (ADCs) to convert the received signal into the digital domain. Our focus is on the case where neither the transmitter nor the receiver have any *a priori* channel state information (CSI), which implies that the channel realizations have to be learned through pilot transmission followed by BS-side channel estimation, based on coarsely quantized observations. We derive a low-complexity channel estimator and present lower bounds and closed-form approximations for the information-theoretic rates achievable with the proposed channel estimator together with conventional linear detection algorithms.

Second, we consider the massive MU-MIMO downlink for the case when the BS uses low-resolution digital-to-analog converters (DACs) to generate the transmit signal. We derive lower bounds and closed-form approximations for the achievable rates with linear precoding under the assumption that the BS has access to perfect CSI. We also propose novel nonlinear precoding algorithms that are shown to significantly outperform linear precoding for the extreme case of 1-bit DACs. Specifically, for the case of symbol-rate 1-bit DACs and frequency-flat channels, we develop a multitude of nonlinear precoders that trade between performance and complexity. We then extend the most promising nonlinear precoders to the case of oversampling 1-bit DACs and orthogonal frequency-division multiplexing for operation over frequency-selective channels.

Third, we extend our analysis to take into account other hardware imperfections such as nonlinear amplifiers and local oscillators with phase noise.

The results in this thesis suggest that the resolution of the ADCs and DACs in massive MU-MIMO systems can be reduced significantly compared to what is used in today's state-of-the-art communication systems, without significantly reducing the overall system performance.

Keywords: Massive multi-user multiple-input multiple-output, analog-to-digital converter, digital-to-analog converter, quantization, hardware impairments, beamforming, channel estimation, linear combing, linear precoding, nonlinear precoding, convex optimization, orthogonal frequency-division multiplexing.

List of Publications

This thesis is based on the following publications:

[A] S. Jacobsson, G. Durisi, M. Coldrey, U. Gustavsson, and C. Studer, "Throughput analysis of massive MIMO uplink with low-resolution ADCs", *IEEE Transactions on Wireless Communications*, vol. 16, no. 6, pp. 4038–4051, Jun. 2017.

[B] S. Jacobsson, G. Durisi, M. Coldrey, T. Goldstein, and C. Studer, "Quantized precoding for massive MU-MIMO," *IEEE Transactions on Communications*, vol. 65, no. 11, pp. 4670–4684, Nov. 2017.

[C] S. Jacobsson, W. Xu, G. Durisi, and C. Studer, "MSE-optimal 1-bit precoding for multiuser MIMO via branch and bound," in *Proceedings of IEEE International Conference on Acoustics, Speech and Signal Processing (ICASSP)*, Calgary, AB, Canada, Apr. 2018, pp. 3589–3593.

[D] S. Jacobsson, G. Durisi, M. Coldrey, and C. Studer, "Linear precoding with low-resolution DACs for massive MU-MIMO-OFDM downlink," *IEEE Transactions on Wireless Communications*, vol. 18, no. 3, pp. 1595–1609, Mar. 2019.

[E] S. Jacobsson, M. Coldrey, G. Durisi, and C. Studer, "On out-of-band emissions of quantized precoding in massive MU-MIMO-OFDM," in *Proceedings of Asilomar Conference on Signals, Systems, and Computers*, Pacific Grove, CA, USA, Oct.– Nov. 2017, pp. 21–26.

[F] S. Jacobsson, O. Castañeda, C. Jeon, G. Durisi, and C. Studer, "Nonlinear precoding for phase-quantized constant-envelope massive MU-MIMO-OFDM," in *Proceedings of IEEE International Conference on Telecommunications (ICT)*, St. Malo, France, Jun. 2018, pp. 367–372.

[G] S. Jacobsson, U. Gustavsson, G. Durisi, and C. Studer, "Massive MU-MIMO-OFDM uplink with hardware impairments: Modeling and analysis," in *Proceedings of Asilomar Conference on Signals, Systems, and Computers*, Pacific Grove, CA, USA, Oct. 2018, pp. 1829–1835.

Publications by the author not included in the thesis:

[H] S. Jacobsson, G. Durisi, M. Coldrey, U. Gustavsson, and C. Studer, "One-bit massive MIMO: Channel estimation and high-order modulations," in *Proceedings of IEEE International Conference on Communications Workshop (ICCW)*, London, U.K., June 2015, pp. 1304–1309.

[I] S. Jacobsson, G. Durisi, M. Coldrey, T. Goldstein, and C. Studer, "Nonlinear 1-bit precoding for massive MU-MIMO with higher-order modulation," in *Proceedings of Asilomar Conference on Signals, Systems, and Computers*, Pacific Grove, CA, USA, Nov. 2016, pp. 763–767.

[J] S. Parkvall *et al.*, "Network architecture, methods, and devices for a wireless communications network," US Patent Application 2017/03157 A1, Nov. 2017, filed May 2016.

[K] S. Parkvall *et al.*, "Network architecture, methods, and devices for a wireless communications network," US Patent Application 2017/031670 A1, Nov. 2017, filed May 2016.

[L] S. Jacobsson, G. Durisi, M. Coldrey, and C. Studer, "Massive MU-MIMO-OFDM downlink with one-bit DACs and linear precoding," in *Proceedings of IEEE Global Communications Conference (GLOBECOM)*, Singapore, Singapore, Dec. 2017.

[M] O. Castañeda, S. Jacobsson, G. Durisi, M. Coldrey, T. Goldstein, and C. Studer, "1-bit massive MU-MIMO precoding in VLSI," *IEEE Journal on Emerging and Selected Topics in Circuits and Systems*, vol. 7, no. 4, pp. 508–522, Dec. 2017.

[N] S. Jacobsson, G. Durisi, M. Coldrey, and C. Studer, "Massive multiuser MIMO downlink with low-resolution converters," in *Proceedings of International Zurich Seminar on Information and Communication (IZS)*, Zurich, Switzerland, Feb. 2018, pp. 53–55.

[O] U. Gustavsson, S. Jacobsson, G. Durisi, V. Björk, M. Coldrey, and L. Sundström, "Wireless communication node and a method for processing a signal in said node," Feb. 2018, US Patent 2018/04837 A1, filed Apr. 2015.

[P] O. Castañeda, S. Jacobsson, G. Durisi, T. Goldstein, and C. Studer, "VLSI design of a 3-bit constant-modulus precoder for massive MU-MIMO," in *IEEE International Symposium on Circuits and Systems (ISCAS)*, Florence, Italy, May 2018.

[Q] S. Jacobsson, Y. Ettefagh, G. Durisi, and C. Studer, "All-digital massive MIMO with a fronthaul constraint," in *Proceedings of IEEE Workshop Statistical Signal Processing Workshop (SSP)*, Freiburg, Germany, Jun. 2018, pp. 218–222.

[R] S. Jacobsson, M. Coldrey, A. Nilsson, and G. Durisi, "Method and apparatus for massive MU-MIMO," Patent Application PCT/EP2018/066414, filed Jun. 2018.

[S] S. Jacobsson, H. Farhadi, S. Rezaei Aghdam, T. Eriksson, and U. Gustavsson, "Beamformed transmission using a precoder," Patent Application PCT/SE2019/050455, filed May 2019.

[T] S. Rezaei Aghdam, S. Jacobsson, and T. Eriksson, "Distortion-aware linear precoding for millimeter-wave multiuser MISO downlink," in *Proceedings of IEEE International Conference on Communications Workshop (ICCW)*, Shanghai, China, May 2019, to appear.

[U] H. Farhadi, U. Gustavsson, and S. Jacobsson, "Link adaptation for spatial multiplexing," Patent Application PCT/SE2019/050557, filed Jun. 2019.

[V] S. Jacobsson, C. Fager, I. C. Sezgin, L. Aabel, and M. Coldrey, "Radio transceiver device configured for dithering of a received signal," Patent Application PCT/SE2019/050638, filed Jun. 2019.

[W] S. Jacobsson, C. Lindquist, G. Durisi, T. Eriksson, and C. Studer, "Timing and frequency synchronization for 1-bit massive MU-MIMO-OFDM downlink," in *Proceedings of IEEE International Workshop on Signal Processing Advances in Wireless Communications (SPAWC)*, Cannes, France, Jul. 2019, to appear.

[X] A. Balatsoukas-Stimming, O. Castañeda, S. Jacobsson, G. Durisi, and C. Studer, "Neural-network optimized 1-bit precoding for massive MU-MIMO," in *Proceedings of IEEE International Workshop on Signal Processing Advances in Wireless Communications (SPAWC)*, Cannes, France, Jul. 2019, to appear.

[Y] Y. Ettefagh, S. Jacobsson, G. Durisi, and C. Studer, "All-digital massive MIMO uplink and downlink rates under a fronthaul constraint," in *Proceedings of Asilomar Conference on Signals, Systems, and Computers*, Pacific Grove, CA, USA, Nov. 2019, to appear.

[Z] O. Castañeda, S. Jacobsson, G. Durisi, T. Goldstein, and C. Studer, "Finite-alphabet Wiener filter precoding for mmWave massive MU-MIMO systems," in *Proceedings of Asilomar Conference on Signals, Systems, and Computers*, Pacific Grove, CA, USA, Nov. 2019, to appear.

[Å] S. Jacobsson, L. Aabel, M. Coldrey, I. C. Sezgin, C. Fager, G. Durisi, and C. Studer, "Massive MU-MIMO-OFDM uplink with direct RF-sampling and 1-bit ADCs," submitted to *IEEE Global Communications Conference (GLOBECOM)*, Waikoloa, HI, USA, Dec. 2019.

Acknowledgements

This thesis would never have been written without the invaluable guidance and support from my colleagues, friends, and family.

First and foremost, I would like to sincerely thank my main supervisor Giuseppe Durisi for giving me the opportunity to pursue a doctoral degree on such an interesting research topic. Your knowledge, attention to details, precise feedback, and constant support are things that I have really appreciated and learned from. I am also very grateful to my co-supervisor Mikael Coldrey for his technical insight, encouragement, and guidance. It is always a pleasure to work (and play floorball) with you. Many thanks also to my (unofficial) co-supervisor Christoph Studer for his hospitality during my visits to Cornell University, and for providing me with an endless stream of ideas to work on and memes to laugh at. I am looking forward to continued fun and fruitful collaboration with you.

I would also like to thank all of my colleagues (past and present) and friends in the Communication Systems group at Chalmers University of Technology, in Wing 62 at Ericsson Lindholmen, and in the VLSI Information Processing group at Cornell University for creating such stimulating work environments. It has been a pleasure to get to know you all. A special thanks goes to Ulf Gustavsson with whom I had the privilege of sharing not only one but two offices with. I have enjoyed all of our discussions and there is seldom a dull moment when you are around. I would also like to especially thank Agneta Kinnander, Anders Aronsson, Andreas Buchberger, Björn Johannisson, Carl Lindquist, Charles Jeon, Christian Fager, Colette O'Meara, Cristian Bogdan Czegledi, Fredrik Athley, Gabriel Garcia, Henrik Sahlin, Johan Östman, Markus Fröhle, Oscar Castañeda, Rahul "Sassy" Devassy, Sina Rezaei Aghdam, Sven "Antenn" Petersson, and Thomas Eriksson, You have all helped me in various ways during these four years and counting.

Last but definitely not least, I would like to express my most sincere gratitude and appreciation to my parents and my two awesome sisters for their continuous support, trust, and encouragement over the years.

<div align="right">

Sven Jacobsson
Gothenburg, Sweden, August 2019

</div>

Acronyms

3GPP	Third Generation Partnership Project
4G	Fourth Generation
5G	Fifth Generation
ACLR	Adjacent Channel Leakage Ratio
ADC	Analog-to-Digital Converter
AWGN	Additive White Gaussian Noise
BER	Bit Error Rate
BS	Base Station
CPRI	Common Public Radio Interface
CSI	Channel State Information
DAC	Digital-to-Analog Converter
DPC	Dirty-Paper Coding
DSP	Digital Signal Processing
EHF	Extremely High Frequency
EMBB	Enhanced Mobile Broadband
ENOB	Effective Number of Bits
FOM	Figure of Merit
FWA	Fixed Wireless Access
ISSCC	International Solid-State Circuit Conference
LMMSE	Linear Minimum Mean Square Error
LNA	Low-Noise Amplifier
LO	Local Oscillator
LTE	Long-Term Evolution
MRC	Maximal-Ratio Combining

MRT	Maximal-Ratio Transmission
MIMO	Multiple-Input Multiple-Output
MMSE	Minimum Mean Square Error
MSE	Mean Square Error
MTC	Machine-Type Communication
MU	Multi-User
NR	New Radio
OFDM	Orthogonal Frequency-Division Multiplexing
OOB	Out-of-Band
OSR	Oversampling Ratio
PA	Power Amplifier
PAPR	Peak-to-Average Power Ratio
PDF	Probability Density Function
PQN	Pseudo-Quantization Noise
PSD	Power Spectral Density
QPSK	Quadrature Phase-Shift Keying
RHS	Right-Hand Side
RF	Radio Frequency
SIC	Successive Interference Cancellation
SINDR	Signal-to-Interference-Noise-and-Distortion Ratio
SINR	Signal-to-Interference-and-Noise Ratio
SHF	Super High Frequency
SNDR	Signal-to-Noise-and-Distortion Ratio
SNR	Signal-to-Noise Ratio
SPS	Samples per Second

SQUID	Squared-Infinity Norm Douglas-Rachford Splitting
SU	Single-User
TDD	Time-Division Duplexing
UE	User Equipment
UHF	Ultra High Frequency
URLLC	Ultra-Reliable Low-Latency Communication
VLSI	Very-Large-Scale Integration
ZF	Zero-Forcing
ZOH	Zero-Order Hold

Contents

D Linear Precoding with Low-Resolution DACs for Massive MU-MIMO-OFDM Downlink   D1

E On Out-of-Band Emissions of Quantized Precoding in Massive MU-MIMO-OFDM   E1

Part I

Overview

Introduction

1.1 Background

Information and communication technologies have enabled a digital transformation of society and industry, making it possible to share information and collaborate on a global scale. Today, we are on the brink of living in a networked society, where everyone and everything that can benefit from being connected will be connected.

Since the emergence of mobile communication in the early 1980s, a new generation of cellular networks has appeared roughly every ten years, leading up to the first commercial deployments of fifth generation (5G) cellular networks in the second quarter of 2019. Fig. 1.1 shows the worldwide number of mobile subscriptions by technology according to the Ericsson Mobility Report [1]. Today, the total number of mobile subscriptions exceeds 7.9 billion (which corresponds to 1.04 mobile subscriptions per capita) with Long-Term Evolution (LTE), used in fourth generation (4G) cellular networks, being the dominant radio-access technology. The radio-access technology embodying 5G is known as New Radio (NR) and was standardized by the third generation partnership project (3GPP) for nonstandalone and standalone operation in 2017 and 2018, respectively [2]. With 5G-compatible mobile devices becoming increasingly available, it is predicted that the number of NR subscriptions will grow rapidly. In fact, the number of NR subscriptions is foreseen to account for over 20 % of all mobile subscriptions by the end of 2024 [1].

With a growing demand for high-speed, ultra-reliable, low-latency, and energy-efficient wireless communications, combined with a crowded radio spectrum, the development of 5G cellular networks is combating a multifaceted challenge. Emerging 5G use cases include autonomous vehicle control, intelligent transport systems, factory automation,
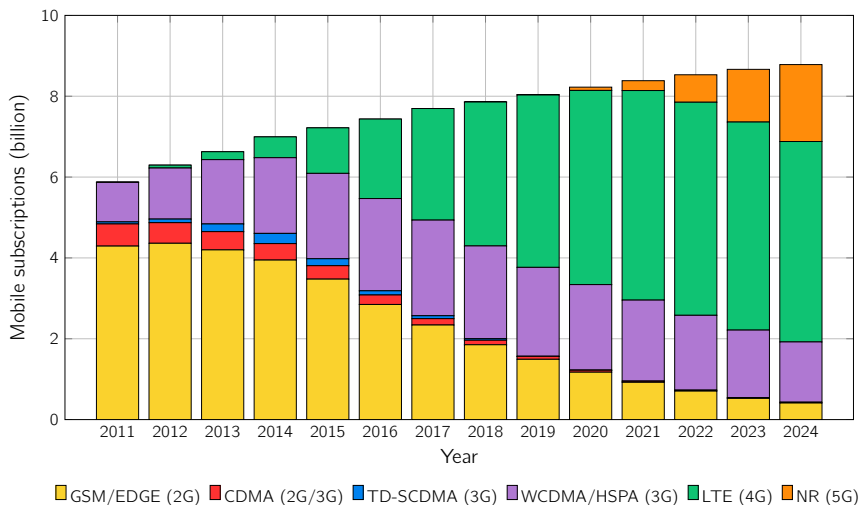
Figure 1.1: Mobile subscriptions by radio access technology (excluding MTC connections and FWA subscriptions) according to the Ericsson Mobility Report [1].

smart grids, high-definition video streaming, augmented and virtual reality, fixed wireless access (FWA) to households, and providing coverage to users in high-mobility scenarios [3, 4]. The use cases targeted by 5G are often categorized into three distinct classes, namely, enhanced mobile broadband (EMBB), massive machine-type communication (MTC), and ultra-reliable low-latency communication (URLLC) [5, 6].

- EMBB is the natural evolution of the existing mobile broadband connectivity provided by today's cellular networks [5]. The goal is to provide enhanced coverage (e.g., to provide a reliable internet connection to spectators in a crowded stadium and to passengers in a high-speed train) and to meet the extreme requirements on data rate and traffic volume put on cellular networks by increased human-centric communication. Demanding EMBB services include high-definition video streaming, social networking, augmented and virtual reality, and online gaming [1].

- Massive MTC involves providing wide-area coverage to a large number (e.g., tens of billions) of low-complexity machine-type devices (e.g., remote sensors, actuators, and wearables), which are assumed to transmit sporadically short data packets [7, 8]. Key requirements include very low device cost and energy consumption, scalability, and deep indoor penetration. Supporting high data rates is, typically, of less importance.
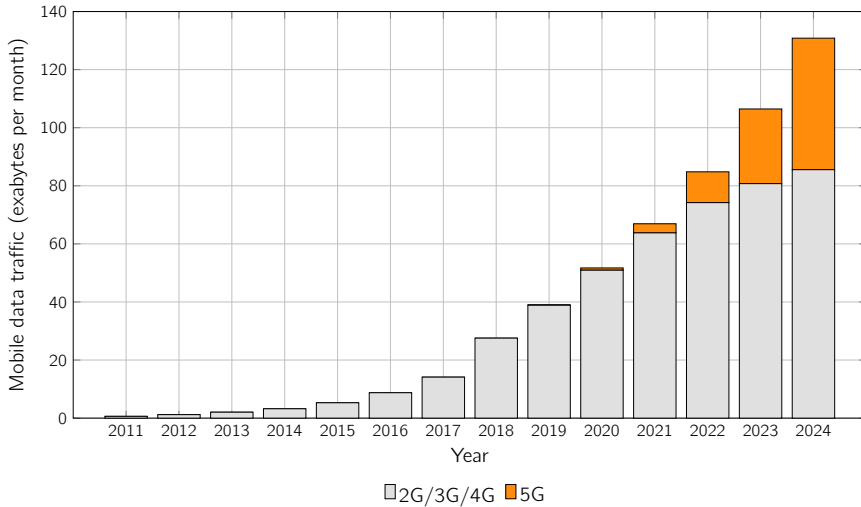
Figure 1.2: Monthly mobile data traffic according to the Ericsson Mobility Report [1].

- URLLC involves providing wireless connectivity to mission-critical applications with stringent requirements on reliability and latency. Use cases that fall into this category include real-time control of manufacturing processes in smart factories, remote medical surgery, and traffic safety [8, 9].

Fig. 1.2 shows a forecast of worldwide monthly data traffic according to the Ericsson Mobility Report [1]. Mobile data traffic is expected to increase by about 30 % annually to surpass 130 exabytes per month by 2024 (with 35 % of this traffic being carried by 5G networks). This immense growth in mobile data traffic is fueled on by the increase in the number of mobile subscriptions (see Fig. 1.1) and by a significant increase in the average data traffic per subscription (for example, the average mobile data traffic per smartphone in 2017 was 2.3 gigabytes per month, compared to 1.6 gigabytes per month in 2016) [10] In order to meet these ever-increasing traffic demands, technologies used in the LTE system embodying 4G must be complemented with a set of new, and possibly disruptive, technologies [11–13]. In particular, to support demanding EMBB services, 5G cellular networks must utilize advanced multi-antenna technologies and support communication over the wide bandwidths available in the millimeter-wave part of the radio spectrum.

The spectrum in the ultra high frequency (UHF) band, ranging from 300 MHz to 3 GHz, used in today's cellular communication systems is becoming increasingly crowded. This has motivated an exploration of the vast amount of underutilized spectrum in the super high frequency (SHF) and extremely high frequency (EHF) bands with frequencies in the millimeter-wave range from 3 GHz to 300 GHz [14]. In fact, the first release of NR already supports operation in both unlicensed and licensed frequency bands from below
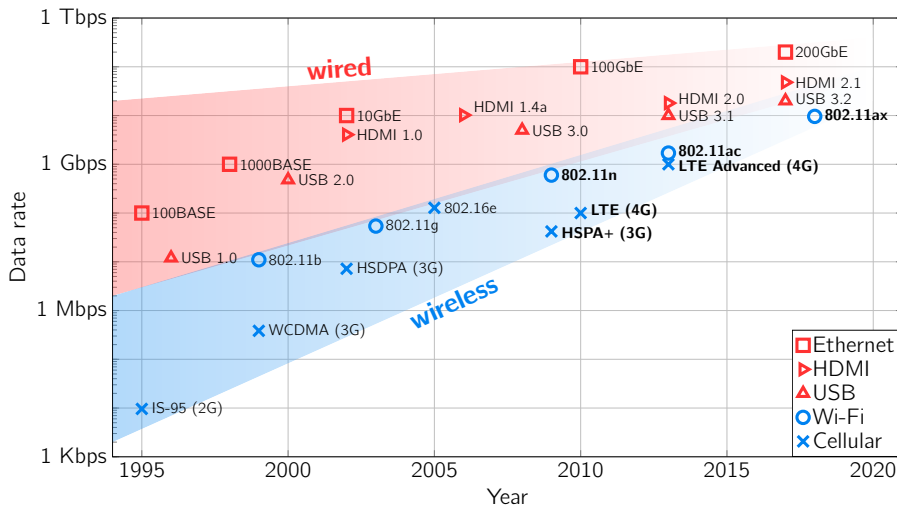
Figure 1.3: Data rates supported in wired and wireless communication standards for consumer electronics [18, Fig, 2.3]. Wireless standards that utilize MIMO technology are written in bold letters.

1 GHz up to 52.6 GHz [6]. Challenges with millimeter-wave cellular communication include propagation issues such as high penetration loss, low diffraction around obstacles, atmospheric absorption, and foliage attenuation [15, 16]. Furthermore, there is an abundance of hardware-related challenges involved with increasing the carrier frequency [17].

Multiple-input multiple-output (MIMO) technology (i.e., using multiple antenna elements at both the transmitter and the receiver) is used in both LTE [19, 20] and NR [2, 5] to improve system performance. MIMO is also a key technology component in modern Wi-Fi standards [21, 22]. Fig. 1.3 shows data rates supported by common wired and wireless communication standards for consumer electronics, as reported in [18, Fig. 2.3]. We note that, in agreement with Edholm's law [23], data rates supported by wireless communication standards are rapidly approaching data rates supported by wired communication standards—MIMO technology has played an integral role in narrowing the gap. Advantages with MIMO technology include robustness towards fading (spatial diversity), directional transmission and reception using beamforming, and improved spectral efficiency by carrying multiple data streams in the same time-frequency resource (spatial multiplexing). Beamforming involves coherently processing the signal at the different antenna elements at the base station (BS) in such a way that the radiated or received energy is focused in a specific direction. Spatial multiplexing can be used for both single-user (SU) and multi-user (MU) communication. In SU-MIMO, the multiple data streams are transmitted to (or received from) a single multi-antenna user equipment (UE). In MU-MIMO, a plurality of single-antenna or multi-antenna UEs are served in the same time-frequency resource.

Equipping the BS with a large number (e.g., in the order of hundreds or even thousands) of active antenna elements compared to the number of UEs—a system architecture solution often referred to as massive MU-MIMO—is a potentially disruptive MU-MIMO technology foreseen to be a key technology component in 5G cellular networks. Massive MU-MIMO promises significant gains in, e.g., spectral efficiency and energy efficiency compared to traditional small-scale SU-MIMO and MU-MIMO systems [24–29]. Furthermore, the large beamforming gain achievable with a massive number of antenna elements will be crucial to counteract the high propagation loss in millimeter-wave systems [30].

Scaling up the number of active antenna elements at the BS will, however, lead to significant increases in radio frequency (RF) circuitry power consumption and system costs unless power-efficient and low-cost hardware components are used [26]. Such low-cost hardware components will, however, reduce the signal quality due to hardware imperfections. There are several hardware imperfections in practical radio transceivers; for example, phase noise in local oscillators (LOs), nonlinearities in power amplifiers (PAs) and low-noise amplifier (LNAs), in-phase/quadrature imbalance in mixers, and quantization noise in data converters. Fortunately, massive MU-MIMO has been shown to exhibit some resilience towards the use of low-precision hardware (see, e.g., [31–36]). Nevertheless, practical deployment of massive MU-MIMO will require novel design approaches that jointly reduce system costs and circuit power consumption, without severely degrading the spectral efficiency and reliability.

1.2 Scope of the Thesis

The specific focus of this thesis is on the impact of using low-resolution data converters in massive MU-MIMO systems. We shall restrict our analysis to the case of homodyne transceivers in which down-conversion of RF signals to baseband and up-conversion of baseband signals to RF is performed in the analog domain using an LO and a mixer [37, Chapter 10]. More specifically, we assume that in the massive MU-MIMO *uplink* (multiple UEs transmit to the BS), a pair of low-resolution analog-to-digital converters (ADCs) is used per antenna at the BS to convert the in-phase and quadrature components of the received analog baseband signal into digital domain. Conversely, in the massive MU-MIMO *downlink* (BS transmits to multiple UEs), a pair of low-resolution digital-to-analog converters (DACs) is used per antenna at the BS to convert the in-phase and quadrature components of the digital transmit baseband signal into analog domain. High-speed and high-resolution data converters are power-hungry devices [38–40]. Hence, architectures involving low-resolution data converters are attractive for massive MU-MIMO systems, where the total number of data converters at the BS could be in the order of hundreds or even thousands. The question at the core of this thesis is whether the aforementioned massive MU-MIMO gains, which were theoretically derived under the assumption of ideal hardware, survive in the presence of significant impairments due to low-resolution data converter solutions.

An alternative to reducing the resolution of the data converters per RF chain in massive MU-MIMO is to instead reduce the number of RF chains and divide the required beamforming between the analog and digital domain [40–42]. In such hybrid-beamforming architectures, a large set of analog phase shifters are connected to a significantly smaller set of data converters [43]. The use of low-resolution data converters combined with hybrid beamforming is considered in [44–46]. Throughout this thesis, we shall exclusively focus on digital-beamforming architectures in which each antenna element is connected to a pair of ADCs and a pair of DACs.

The specific objectives of this thesis can be summarized as follows.

    I To characterize the uplink throughput achievable in a massive MU-MIMO system for scenarios in which the BS employs low-resolution ADCs.

   II To design low-complexity channel estimation and data detection algorithms that, together with modern coding techniques, are able to approach the uplink throughput unveiled in Objective I.

  III To characterize the downlink throughput achievable in a massive MU-MIMO system for scenarios in which the BS employs low-resolution DACs.

  IV To develop low-complexity precoding algorithms that, together with modern coding techniques, are able to approach the downlink throughput unveiled in Objective III.

1.3 Organization of the Thesis

This thesis is formatted as a collection of papers and divided into two parts. Part I serves as an introduction to Part II consisting of the included papers. The remainder of Part I of the thesis is organized as follows. A brief introduction to the massive MU-MIMO uplink and downlink is provided in Chapter 2. In Chapter 3, the basic building blocks of an ADC and a DAC are introduced, and the operation of a quantizer is explained in detail. Bussgang's theorem, which is a useful tool for analyzing the impact of nonlinearities in massive MU-MIMO systems, is introduced in Chapter 4. Chapter 5 introduces the massive MU-MIMO uplink and downlink for the case when low-resolution data converters are used at the BS. Finally, the contributions of the included papers are summarized in Chapter 6.

1.4 Notation

This section describes the notation used in Part I of this thesis. Lowercase and uppercase boldface letters designate column vectors and matrices, respectively. The identity matrix of size $M \times M$ is denoted by $\mathbf{I}_M$ and the $M \times N$ all-zeros matrix is denoted by $\mathbf{0}_{M \times N}$.

For a matrix $\mathbf{A}$, its complex conjugate, transpose, and Hermitian transpose is denoted $\mathbf{A}^*$, $\mathbf{A}^T$, and $\mathbf{A}^H$, respectively. The trace and the main diagonal of $\mathbf{A}$ are denoted by $\text{tr}(\mathbf{A})$ and $\text{diag}(\mathbf{A})$, respectively. The $M \times M$ matrix $\text{diag}(\mathbf{a})$ is diagonal with the elements of the M-dimensional vector $\mathbf{a}$ along its main diagonal. The determinant of $\mathbf{A}$ is denoted by $\det(\mathbf{A})$. We use $\mathbf{A} \succeq \mathbf{0}_{M \times M}$ to indicate that the $M \times M$ matrix $\mathbf{A}$ is positive semidefinite. The floor function $\lfloor r \rfloor$ produces the largest integer less than or equal to $r \in \mathbb{R}$. We use $\text{sgn}(\,\cdot\,)$ to denote the signum function, which is applied element-wise to vectors and defined as $\text{sgn}(r) = 1$ if $r \geq 0$ and $\text{sgn}(r) = -1$ if $r < 0$. We further use $\mathbb{1}_{\mathcal{A}}(a)$ to denote the indicator function, which is defined as $\mathbb{1}_{\mathcal{A}}(a) = 1$ for $a \in \mathcal{A}$ and $\mathbb{1}_{\mathcal{A}}(a) = 0$ for $a \notin \mathcal{A}$. The real and the imaginary parts of a complex vector $\mathbf{a}$ are denoted by $\Re\{\mathbf{a}\}$ and $\Im\{\mathbf{a}\}$, respectively. The ℓ_2-norm of a vector $\mathbf{a}$ is denoted by $\|\mathbf{a}\|_2$. The real-valued zero-mean Gaussian distribution with covariance $\mathbf{R} \in \mathbb{R}^{M \times M}$ is denoted by $\mathcal{N}(\mathbf{0}_{M \times 1}, \mathbf{R})$. The complex-valued circularly symmetric Gaussian distribution with covariance $\mathbf{C} \in \mathbb{C}^{M \times M}$ is denoted by $\mathcal{CN}(\mathbf{0}_{M \times 1}, \mathbf{C})$. The uniform distribution on the interval (a, b) is denoted by $\mathcal{U}(a, b)$. The probability density function (PDF) of a continuous random variable x is written as f_x, the joint PDF of two continuous random variables x and y is written as $f_{x,y}$, and the conditional PDF of y given x is written as $f_{y|x}$. For two continuous random variables x and y with corresponding PDFs f_x and f_y, the Kullback-Leibler divergence between f_x and f_y is $\mathcal{D}(f_x \| f_y) = \int_{-\infty}^{\infty} f_x(\omega) \log_2(f_x(\omega)/f_y(\omega)) \, \mathrm{d}\omega$. The mutual information between two random variables x and y is $\mathcal{I}(x; y) = \mathcal{D}(f_{x,y} \| f_x f_y)$. The binary entropy function is $\mathcal{H}(\epsilon) = -\epsilon \log_2(\epsilon) - (1 - \epsilon) \log_2(1 - \epsilon)$. The cumulative distribution function of the standard normal distribution is $\Phi(x) = \frac{1}{\sqrt{2\pi}} \int_{-\infty}^{x} \exp(-u^2/2) \, \mathrm{d}u$. Finally, we use $\mathbb{E}_x[\,\cdot\,]$ to denote expectation with respect to the random variable x.

CHAPTER 2

Fundamentals of Massive MU-MIMO

In this chapter, we introduce the basics of massive MU-MIMO uplink and downlink communications. A single-cell massive MU-MIMO system, as illustrated in Fig. 2.1, is considered. The system consists of a BS with B antennas that simultaneously serves $U \leq B$ single-antenna UEs in the same time-frequency resource using spatial multiplexing. Throughout this chapter, we shall assume, for simplicity, that the system operates over a frequency-flat channel and that all hardware components, including the ADCs and DACs, are ideal. The wireless channel connecting the UEs to the BS is modeled as memoryless block-fading channel, i.e., a channel that remains constant during a coherence interval of $T = t_{\mathrm{coh}} f_{\mathrm{coh}}$ consecutive symbol transmissions (channel uses), before changing into a new independent realization. Here, t_{coh} is the coherence time (measured in seconds) and f_{coh} is the coherence bandwidth (measured in Hertz). The average number of bits conveyed during a channel use is denoted by R and is called the *rate* (measured in bits per channel use or, equivalently, in bits per second per Hertz). A rate R is said to be achievable if there exist a sequence of codes operating at rate R for which the average error probability tends to zero as the length of the codewords tends to infinity. The channel capacity is defined as the supremum of all achievable rates [47, Chapter 3].

The rest of this chapter is organized as follows. In Sec. 2.1, we introduce the time-division duplexing (TDD) scheme used to separate uplink and downlink transmissions. In Sec. 2.2, we introduce the massive MU-MIMO uplink system model and provide the sum rate achievable with linear combing, Gaussian signaling, and perfect BS-side channel state information (CSI). In Sec. 2.3, we introduce the massive MU-MIMO downlink system model and provide the sum rate achievable with linear precoding, Gaussian signaling, and perfect BS-side CSI. Finally, we discuss channel estimation in Sec. 2.4.
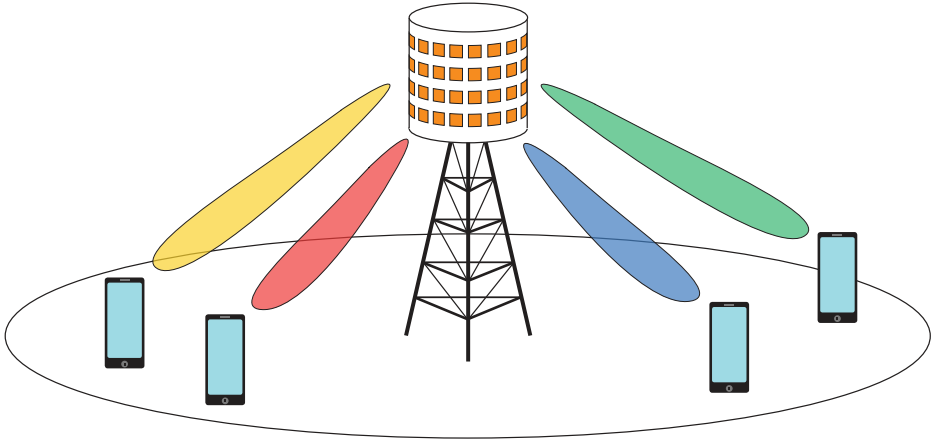
Figure 2.1: A single-cell multiuser MIMO system where U single-antenna UEs are served by a B-antenna BS in the same time-frequency resource through spatial multuplexing.

2.1 Time-Division Duplexing

Throughout the thesis, it is assumed that the system operates in TDD mode, which implies that uplink and downlink transmissions take place in the same frequency spectrum but in different time slots. The TDD frame structure is illustrated in Fig. 2.2. We use T^{ul} and T^{dl} (for which it holds that $T^{\mathrm{ul}} + T^{\mathrm{dl}} = T$) to denote the number of symbols transmitted during the uplink and downlink phase, respectively. In every coherence interval, the UEs transmit $T_{\mathrm{p}}^{\mathrm{ul}} \geq U$ pilot symbols (which are known to the BS) and $T_{\mathrm{d}}^{\mathrm{ul}}$ data symbols during the uplink phase (where $T_{\mathrm{p}}^{\mathrm{ul}} + T_{\mathrm{d}}^{\mathrm{ul}} = T^{\mathrm{ul}}$). The pilot symbols allow the BS to acquire CSI, which, in turn, is used for detecting the data symbols. The CSI is also used for precoding the T^{dl} data symbols transmitted from the BS to the UEs during the downlink phase.

2.2 Uplink Transmission

The discrete-time complex baseband signal received over the B BS antennas during the uplink phase of an arbitrary coherence interval can be written as

$$\mathbf{y}^{\mathrm{ul}}[n] = \mathbf{H}\,\mathbf{s}^{\mathrm{ul}}[n] + \mathbf{w}^{\mathrm{ul}}[n] \tag{2.1}$$
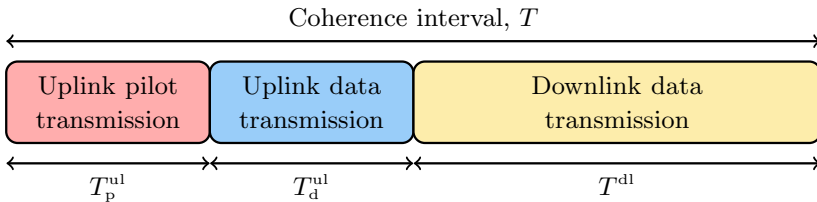
Figure 2.2: TDD frame structure. The UEs transmit pilots and data symbols in the uplink. The BS transmits data symbols in the downlink.

for $n = 0, 1, \ldots, T^{\mathrm{ul}} - 1$. Here, the vector $\mathbf{s}^{\mathrm{ul}}[n] = \left[s_1^{\mathrm{ul}}[n], s_2^{\mathrm{ul}}[n], \ldots, s_U^{\mathrm{ul}}[n]\right]^T \in \mathbb{C}^U$, which have independent and identically distributed entries, contains the symbols transmitted from all UEs. The transmitted symbols satisfies the average power constraint $\mathbb{E}\left[|s_u^{\mathrm{ul}}[n]|^2\right] = P^{\mathrm{ul}}$ for $u = 1, 2, \ldots, U$, where P^{ul} is the UE transmit power. The vector $\mathbf{w}^{\mathrm{ul}}[n] \sim \mathcal{CN}\left(\mathbf{0}_{B \times 1}, N_0^{\mathrm{ul}}\mathbf{I}_B\right)$ is the BS-side additive white Gaussian noise (AWGN), where N_0^{ul} is the one-sided power spectral density (PSD) of the AWGN. Furthermore, $\mathbf{H} \in \mathbb{C}^{B \times U}$ is the channel matrix. In what follows, we model the entries of $\mathbf{H}$ as independent and $\mathcal{CN}(0, 1)$-distributed (Rayleigh fading).

In this section, we shall assume that the BS has noncausal access to perfect CSI, i.e., the BS knows perfectly the realizations of the channel matrix $\mathbf{H}$. This assumption is reasonable only for very long coherence intervals, for which the pilot overhead can be neglected. For shorter coherence intervals, more pilot symbols will have to be transmitted to keep up-to-date with the time-varying channel. In this case, the rate loss associated with the transmission of pilots can not be neglected and perfect CSI can not be guaranteed.

With perfect CSI at the BS, the ergodic sum-rate capacity of the channel input-output model (2.1) is [48, Chapter 10]

$$C^{\mathrm{ul}} = \mathbb{E}_{\mathbf{H}}\left[\log_2\left(\det\left(\mathbf{I}_B + \mathrm{SNR}^{\mathrm{ul}}\,\mathbf{H}\mathbf{H}^H\right)\right)\right] \tag{2.2}$$

where $\mathrm{SNR}^{\mathrm{ul}} = P^{\mathrm{ul}}/N_0^{\mathrm{ul}}$ is the uplink signal-to-noise ratio (SNR).

The sum-rate capacity in (2.2) can be achieved by performing minimum mean-square error (MMSE) together with successive interference cancellation (SIC) at the BS. Unfortunately, the computational complexity associated with implementing MMSE-SIC is prohibitively high, especially for massive MU-MIMO systems that simultaneously serve several UEs using a large number of BS antennas. Linear combining algorithms—although inferior to nonlinear processing algorithms such as MMSE-SIC—are less computationally demanding and, as will be shown next, yield near-optimal performance when the number of BS antennas exceed by far the number of UEs. With linear combining at the BS, an estimate $\mathbf{z}^{\mathrm{ul}}[n] = \left[z_1^{\mathrm{ul}}[n], z_2^{\mathrm{ul}}[n], \ldots, z_U^{\mathrm{ul}}[n]\right]^T \in \mathbb{C}^U$ of the transmitted symbols $\mathbf{s}^{\mathrm{ul}}[n]$ is

obtained as follows:

$$\mathbf{z}^{\mathrm{ul}}[n] = \mathbf{A}\mathbf{y}^{\mathrm{ul}}[n]. \tag{2.3}$$

Here, $\mathbf{A} \in \mathbb{C}^{U \times B}$ is the combing matrix. It follows from (2.1) and (2.3) that

$$z_u^{\mathrm{ul}}[n] = \mathbf{a}_u^T \mathbf{h}_u s_u^{\mathrm{ul}}[n] + \sum_{v \neq u} \mathbf{a}_u^T \mathbf{h}_v s_v^{\mathrm{ul}}[n] + \mathbf{a}_u^T \mathbf{w}^{\mathrm{ul}}[n] \tag{2.4}$$

for $u = 1, 2, \ldots, U$. Here, $\mathbf{h}_u \in \mathbb{C}^B$ is the uth column of $\mathbf{H}$ and $\mathbf{a}_u \in \mathbb{C}^B$ is the uth column of $\mathbf{A}^T$. The first term on the right-hand side (RHS) of (2.4) corresponds to the desired signal; the second term captures the MU interference; the third term corresponds to the AWGN.

It can be shown (see, e.g., [49, Eq. (12)]) that the sum rate achievable with Gaussian signaling and linear combing is

$$R^{\mathrm{ul}} = \sum_{u=1}^{U} \mathbb{E}_{\mathbf{H}} \left[\log_2 \left(1 + \mathrm{SINR}_u^{\mathrm{ul}} \right) \right] \tag{2.5}$$

where

$$\mathrm{SINR}_u^{\mathrm{ul}} = \frac{\mathrm{SNR}^{\mathrm{ul}} \left| \mathbf{a}_u^T \mathbf{h}_u \right|^2}{\mathrm{SNR}^{\mathrm{ul}} \sum_{v \neq u} \left| \mathbf{a}_u^T \mathbf{h}_v \right|^2 + \|\mathbf{a}_u\|_2^2} \tag{2.6}$$

is the uplink signal-to-interference-and-noise ratio (SINR) for the uth UE.

Three conventional linear combining schemes are maximal-ratio combing (MRC), zero-forcing (ZF) combing, and linear minimum mean-square error (LMMSE) combing [49]. The combing matrices associated with these schemes are

$$\mathbf{A} = \begin{cases} \mathbf{H}^H, & \text{for MRC} \\ \left(\mathbf{H}^H \mathbf{H} \right)^{-1} \mathbf{H}^H, & \text{for ZF} \\ \left(\mathbf{H}^H \mathbf{H} + \frac{1}{\mathrm{SNR}^{\mathrm{ul}}} \mathbf{I}_U \right)^{-1} \mathbf{H}^H, & \text{for LMMSE.} \end{cases} \tag{2.7}$$

In Fig. 2.3, the sum rate achievable with Gaussian signaling and linear combing (2.5) is shown as a function of the number of BS antennas B for the case $U = 10$ UEs and $\mathrm{SNR}^{\mathrm{ul}} = 0$ dB. For reference, the rate achievable with MMSE-SIC (2.2) is also shown. Note that the rate achievable with ZF and LMMSE approaches the rate achievable with MMSE-SIC as the number of antennas grow large. This demonstrates that linear combing achieves near-optimal performance in the massive MU-MIMO uplink.

Figure 2.3: Uplink throughput for the case $\mathrm{SNR}^{\mathrm{ul}} = 0$ dB and $U = 10$ UEs. As the number of BS antennas grow large, linear detection offers near-optimal performance.

2.3 Downlink Transmission

The discrete-time complex baseband signal received at the U UEs antennas during the downlink phase of an arbitrary coherence interval can be written as

$$\mathbf{y}^{\mathrm{dl}}[n] = \mathbf{H}^T \mathbf{x}^{\mathrm{dl}}[n] + \mathbf{w}^{\mathrm{dl}}[n] \tag{2.8}$$

for $n = 0, 1, \ldots, T^{\mathrm{dl}} - 1$. Here, $\mathbf{y}^{\mathrm{dl}}[n] = \left[y_1^{\mathrm{dl}}[n], y_2^{\mathrm{dl}}[n], \ldots, y_U^{\mathrm{dl}}[n]\right]^T \in \mathbb{C}^U$ is the received signal at the U UEs and $\mathbf{w}^{\mathrm{dl}}[n] \sim \mathcal{CN}(\mathbf{0}_{U \times 1}, N_0^{\mathrm{dl}} \mathbf{I}_U)$ is the AWGN at the UEs, where N_0^{dl} is the one-sided PSD of the AWGN. The transmitted signal over the B BS antennas, $\mathbf{x}^{\mathrm{dl}}[n] \in \mathbb{C}^B$, must satisfy the average power constraint

$$\mathbb{E}_{\mathbf{H}}\left[\|\mathbf{x}^{\mathrm{dl}}[n]\|_2^2\right] \leq P^{\mathrm{dl}}. \tag{2.9}$$

The capacity of the multiuser downlink channel has been characterized in [50–53]. When perfect CSI is available at the BS, dirty-paper coding (DPC) [54] is known to achieve the sum-rate capacity of the channel (2.8). The ergodic sum-rate capacity of the channel input-output model (2.8) is [55, Eq. (5)]

$$C^{\mathrm{dl}} = \mathbb{E}_{\mathbf{H}}\left[\sup_{\mathrm{diag}(\mathbf{t}) \succeq \mathbf{0}_{U \times U}, \, \|\mathbf{t}\|_2^2 \leq 1} \log_2\left(\det\left(\mathbf{I}_B + \mathrm{SNR}^{\mathrm{dl}} \, \mathbf{H} \, \mathrm{diag}(\mathbf{t}) \mathbf{H}^H\right)\right)\right] \tag{2.10}$$

where $\mathrm{SNR}^{\mathrm{dl}} = P^{\mathrm{dl}}/N_0^{\mathrm{dl}}$ is the downlink SNR.

Practical implementations of DPC (see, e.g., [56–58]) are, however, computationally demanding, with a complexity that scales unfavorably with the number of BS antennas.

Linear precoding on the other hand, is an attractive low-complexity approach to massive MU-MIMO precoding, which offers competitive performance to DPC for large antenna arrays [25]. With linear precoding, the transmitted signal can be written as

$$\mathbf{x}^{\mathrm{dl}}[n] = \alpha \mathbf{P} \mathbf{s}^{\mathrm{dl}}[n] \tag{2.11}$$

where $\mathbf{P} \in \mathbb{C}^{B \times U}$ is the precoding matrix and $\mathbf{s}^{\mathrm{dl}}[n] = \left[s_1^{\mathrm{dl}}[n], s_2^{\mathrm{dl}}[n], \ldots, s_U^{\mathrm{dl}}[n] \right]^T \in \mathbb{C}^U$, where $s_u^{\mathrm{dl}}[n]$ is the symbol intended for the uth UE. These symbols are mutually orthogonal and adhere to the average power constraint $\mathbb{E}\left[|s_u[n]|^2\right] = P^{\mathrm{dl}}$ for $u = 1, 2, \ldots, U$. Furthermore, $\alpha \in \mathbb{R}$ is chosen to satisfy the power constraint (2.9), i.e.,

$$\alpha = \mathbb{E}_{\mathbf{H}}\left[\mathrm{tr}\left(\mathbf{P}\mathbf{P}^H\right)\right]^{-1/2}. \tag{2.12}$$

It follows from (2.8) and (2.11) that

$$y_u^{\mathrm{dl}}[n] = \alpha \mathbf{h}_u^T \mathbf{p}_u s_u^{\mathrm{dl}}[n] + \sum_{v \neq u} \alpha \mathbf{h}_u^T \mathbf{p}_v s_v^{\mathrm{dl}}[n] + w_u^{\mathrm{dl}}[n] \tag{2.13}$$

for $u = 1, 2, \ldots, U$. Here, $\mathbf{p}_u \in \mathbb{C}^B$ corresponds to the uth column of the precoding matrix $\mathbf{P}$. The first term on the RHS of (2.13) corresponds to the desired signal; the second term captures the MU interference; the third term corresponds to the AWGN. It can be shown (see, e.g., [59, Eq. (12)]) that the ergodic sum-rate achievable with Gaussian signaling and linear precoding is

$$R^{\mathrm{dl}} = \mathbb{E}_{\mathbf{H}}\left[\sum_{u=1}^{U} \log_2\left(1 + \mathrm{SINR}_u^{\mathrm{dl}}\right) \right] \tag{2.14}$$

where

$$\mathrm{SINR}_u^{\mathrm{dl}} = \frac{\mathrm{SNR}^{\mathrm{dl}}\left|\mathbf{h}_u^T \mathbf{p}_u\right|^2}{\mathrm{SNR}^{\mathrm{dl}} \sum_{v \neq u}\left|\mathbf{h}_u^T \mathbf{p}_v\right|^2 + 1/\alpha^2} \tag{2.15}$$

is the downlink SINR for the uth UE. Here, we have assumed that the effective channel gain $\alpha \mathbf{h}_u^T \mathbf{p}_u \in \mathbb{C}$ in (2.13) is known to the uth UE.

Three conventional linear precoders are maximal-ratio transmission (MRT), ZF precoding, and LMMSE precoding. The precoding matrices associated with these linear precoders are

$$\mathbf{P} = \begin{cases} \mathbf{H}^*, & \text{for MRT} \\ \mathbf{H}^*\left(\mathbf{H}^T\mathbf{H}^*\right)^{-1}, & \text{for ZF} \\ \mathbf{H}^*\left(\mathbf{H}^T\mathbf{H}^* + \frac{U}{\mathrm{SNR}^{\mathrm{dl}}}\mathbf{I}_U\right)^{-1}, & \text{for LMMSE.} \end{cases} \tag{2.16}$$

In Fig. 2.4, the sum-rate achievable with linear precoding (2.14) is shown as a function
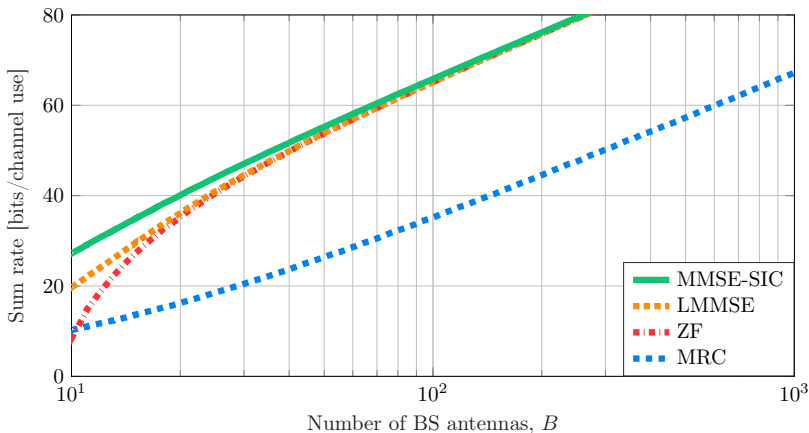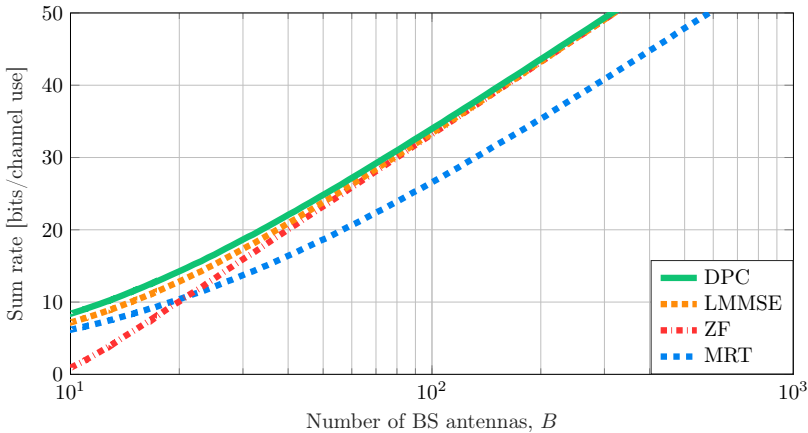
Figure 2.4: Downlink throughput for the case $\mathrm{SNR}^{\mathrm{dl}} = 0$ dB and $U = 10$ UEs. As the number of BS antennas grow large, linear precoding offers near-optimal performance.

of the number of BS antennas B for the case $U = 10$ and $\mathrm{SNR}^{\mathrm{dl}} = 0$ dB. For reference, the rate achievable with DPC (2.10) is also shown (for the case of equal power allocation to the UEs). As the number of BS antennas grow large, the rate achievable with ZF and LMMSE precoding approaches the rate achievable with DPC, which demonstrates that linear precoding is near-optimal for large antenna arrays.

2.4 Channel Estimation

The uplink and downlink rates reported in (2.2), (2.5), (2.10), and (2.14) are valid for the case of perfect CSI at the BS. In practice, however, the channel realizations are not known *a priori* to the BS. Therefore, $T_{\mathrm{p}}^{\mathrm{ul}} \geq U$ symbol transmissions are reserved for the transmission of pilot symbols, which are used at the BS to perform channel estimation. Let $\mathbf{S} = \left[\mathbf{s}^{\mathrm{ul}}[0], \mathbf{s}^{\mathrm{ul}}[1], \ldots, \mathbf{s}^{\mathrm{ul}}[T_{\mathrm{p}}^{\mathrm{ul}} - 1]\right] \in \mathbb{C}^{U \times T_{\mathrm{p}}^{\mathrm{ul}}}$ denote the pilot symbols transmitted from the U UEs during the uplink training phase. The pilot sequences used by the different UEs are typically assumed to be mutually orthogonal, such that

$$\mathbf{S}\mathbf{S}^H = T_{\mathrm{p}}^{\mathrm{ul}} P^{\mathrm{ul}} \mathbf{I}_{U \times U}. \tag{2.17}$$

With this assumption, the LMMSE estimate of $\mathbf{H}$ is given by (see, e.g., [28, Sec. 3.1])

$$\mathbf{H}^{\mathrm{est}} = \frac{1}{T_{\mathrm{p}}^{\mathrm{ul}} P^{\mathrm{ul}} + N_0^{\mathrm{ul}}} \mathbf{Y}\mathbf{S}^H \tag{2.18}$$

where $\mathbf{Y} = \mathbf{HS} + \mathbf{W}$ and $\mathbf{W} = \left[\mathbf{w}^{\mathrm{ul}}[0], \mathbf{w}^{\mathrm{ul}}[1], \ldots, \mathbf{w}^{\mathrm{ul}}[T_{\mathrm{p}}^{\mathrm{ul}} - 1]\right] \in \mathbb{C}^{B \times T_{\mathrm{p}}^{\mathrm{ul}}}$. It follows that the channel matrix $\mathbf{H}$ can be decomposed as (see, e.g., [60, Chapter 12])

$$\mathbf{H} = \mathbf{H}^{\mathrm{est}} + \mathbf{E} \tag{2.19}$$

where the channel estimation error $\mathbf{E} \in \mathbb{C}^{B \times U}$, which has independent and identically distributed $\mathcal{CN}(0, N_0^{\mathrm{ul}}/(T_{\mathrm{p}}^{\mathrm{ul}} P^{\mathrm{ul}} + N_0^{\mathrm{ul}}))$ elements, is uncorrelated with the channel estimate $\mathbf{H}^{\mathrm{est}}$. Note that channel estimation is performed separately at each antenna element. Hence, the quality of the channel estimate improves with the number of pilot symbols and with the SNR, but not with the number of antenna elements.

The channel estimate $\mathbf{H}^{\mathrm{est}}$ is used instead of $\mathbf{H}$ to compute the linear combining matrix in (2.7) and the linear precoding matrix in (2.16), which will, inevitably, reduce the achievable rate since the channel estimates are not perfect. Furthermore, the pilot overhead will incur additional rate loss. Uplink and downlink rates achievable with imperfect CSI and linear processing have been reported in, e.g., [49, 59].

The results in this chapter are valid for massive MU-MIMO systems that are equipped with ideal hardware components. In practice, however, massive MU-MIMO systems will have to make use of nonideal hardware components, which will reduce the signal quality due to hardware impairments. For the remainder of the thesis, it will be assumed that the BS is equipped with low-resolution ADCs and DACs.

Data Converters

Digital signal processing (DSP) is an integral part of all modern cellular systems. In the massive MU-MIMO uplink, in order to process data digitally, the analog signal received at each BS antenna is converted into the digital domain—a process that involves discretization in both time and amplitude. The device that performs these operations is called an ADC. Conversely, in the massive MU-MIMO downlink, the digital representation of the transmit signal at each BS antenna is converted into an analog waveform by a DAC before being transmitted over the wireless channel.

3.1 Quantization

The process of converting a continuous-amplitude signal into a discrete-amplitude signal is known as *quantization*. We define a Q-bit quantizer by a set of 2^Q quantization labels $\mathcal{L} = \{\ell_0, \ell_1, \ldots, \ell_{2^Q-1}\}$ and a set of $2^Q + 1$ quantization thresholds $\mathcal{T} = \{\tau_0, \tau_1, \ldots, \tau_{2^Q}\}$, where $-\infty = \tau_0 < \tau_1 < \cdots < \tau_{2^Q} = \infty$. Let $y \in \mathbb{R}$ denote the input to the quantizer and let $r \in \mathcal{L}$ denote the corresponding output. The output of the quantizer is

$$r = \mathcal{Q}_{\mathbb{R}}(y) \tag{3.1}$$

where

$$\mathcal{Q}_{\mathbb{R}}(y) = \sum_{q=0}^{2^Q-1} \ell_q \mathbb{1}_{[\tau_q, \tau_{q+1})}(y) \tag{3.2}$$

(a) 1-bit quantizer.   **(b)** 3-bit uniform quantizer.   **(c)** 3-bit nonuniform quantizer.
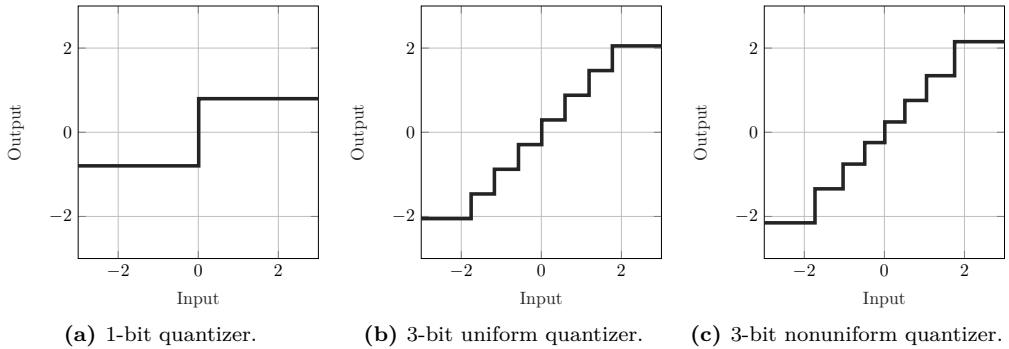
Figure 3.1: Input-output relation for (a) a 1-bit quantizer, (b) a 3-bit uniform quantizer, and (c) a 3-bit nonuniform quantizer.

denotes the real-valued quantization function, which is applied element-wise to vectors.

The quantizer is said to be symmetric and *uniform* if the quantization labels are $\ell_q = \Delta\left(q - 2^{Q-1} + 1/2\right)$ for $q = 0, 1, \ldots, 2^Q - 1$ and if the quantization thresholds are $\tau_q = \Delta\left(q - 2^{Q-1}\right)$ for $q = 1, 2, \ldots, 2^Q - 1$. Here, Δ is the *step size* of the uniform quantizer. If these conditions are not fulfilled, the quantizer is said to be *nonuniform*. For uniform quantizers, the quantization function in (3.2) simplifies to

$$
\mathcal{Q}_{\mathbb{R}}(y) = \begin{cases} \frac{\Delta}{2}\left(1 - 2^Q\right), & \text{if } y < -\gamma \\ \Delta\left\lfloor \frac{y}{\Delta} + \frac{1}{2} \right\rfloor, & \text{if } 2^Q \text{ is odd and } |y| < \gamma \\ \Delta\left\lfloor \frac{y}{\Delta} \right\rfloor + \frac{\Delta}{2}, & \text{if } 2^Q \text{ is even and } |y| < \gamma \\ \frac{\Delta}{2}\left(2^Q - 1\right), & \text{if } y > \gamma. \end{cases} \tag{3.3}
$$

Here, $\gamma = \Delta 2^{Q-1}$ is the *clipping level* of the uniform quantizer. If the number of quantization labels is odd, the uniform quantizer has a label at zero and is called a *midtread* quantizer. If the number of quantization levels is even, the uniform quantizer has a threshold at zero and is called a *midrise* quantizer. For the extreme case of 1-bit quantization, the quantization function in (3.3) reduces to

$$
\mathcal{Q}_{\mathbb{R}}(y) = \frac{\Delta}{2}\,\text{sgn}(y). \tag{3.4}
$$

Fig. 3.1 shows the input-output relation for a 1-bit quantizer (Fig. 3.1a), a 3-bit uniform quantizer (Fig. 3.1b), and a 3-bit nonuniform quantizer (Fig. 3.1c).

The process of mapping a continuous-amplitude signal into a finite set of quantization labels will inevitably introduce a quantization error

$$
e = r - y. \tag{3.5}
$$

Table 3.1: MSE-optimal step size for a $\mathcal{N}(0,1)$-distributed input.

Number of bits, Q	1	2	3	4	5	6
Step size, Δ	1.596	0.9957	0.5860	0.3352	0.1880	0.1040
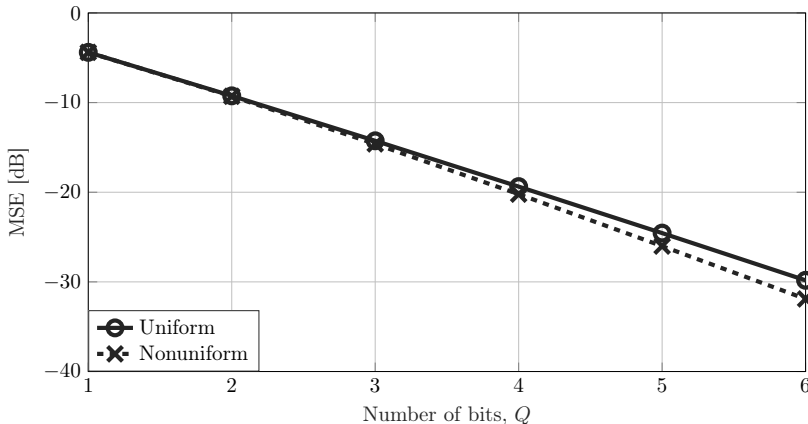
Figure 3.2: MSE after uniform and nonuniform quantization of a $\mathcal{N}(0,1)$-distributed input.

The step size Δ impacts the amount of error caused by a uniform quantizer. If Δ is too small, then there will be significant *overload* distortion (i.e., the error $|e| > \Delta/2$ caused by inputs for which it holds that $|y| > \gamma$). On the other hand, if Δ is too large, then there will be excessive *granular* distortion (i.e., the error $|e| \leq \Delta/2$ caused by inputs for which it holds that $|y| \leq \gamma$). The mean square error (MSE) between the quantizer input and output is defined as $\text{MSE} = \mathbb{E}_y\big[(r-y)^2\big]$. The MSE-optimal choice of step size depends on the PDF of the input to the quantizer [61]. In this work, we shall commonly consider quantization of Gaussian signals. For Gaussian-distributed inputs, the step size that minimizes the MSE is, in general, not available in closed form but can easily be found using numerical methods (see, e.g., [62, 63]). Table 3.1 lists the MSE-optimal step size for $y \sim \mathcal{N}(0,1)$ and for $Q \in \{1, 2, \dots, 6\}$.

At this point, it is important to note that uniform quantizers are, in general, suboptimal. To demonstrate this, we show in Fig. 3.2 the MSE after uniform and nonuniform quantization of a $\mathcal{N}(0,1)$-distributed input. For the case of uniform quantization, the step size is set according to Table 3.1. For the case of nonuniform quantization, the MSE-optimal set of quantization labels $\mathcal{L}$ and quantization thresholds $\mathcal{T}$ are obtained using the Lloyd-Max algorithm [63, 64]. It becomes clear that the performance gap between uniform quantization and nonuniform quantization grows larger as the number of bits increase. However, for low-resolution (e.g., 1–3 bits) quantizers, nonuniform quantization offers only marginal improvements compared to uniform quantization.

(a) 1-bit quantizer. **(b)** 2-bit uniform quantizer. **(c)** 3-bit uniform quantizer.
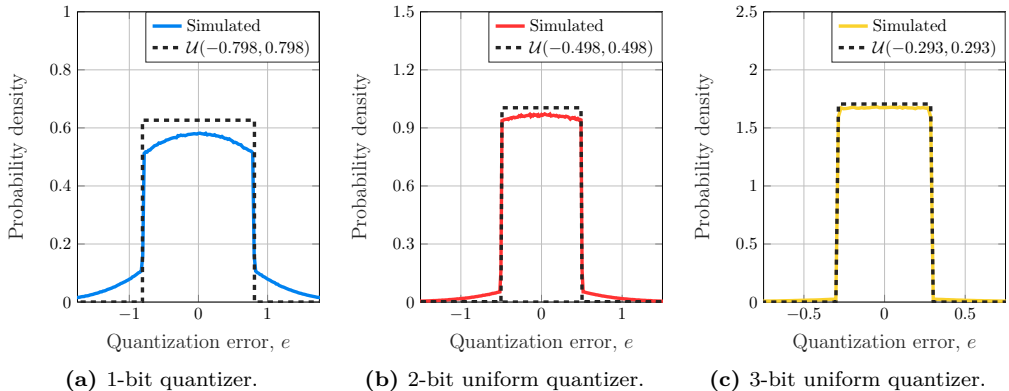
Figure 3.3: PDF of the quantization error for a $\mathcal{N}(0,1)$-distributed input. Approximating the quantization error as a uniformly distributed random variable becomes increasingly accurate as the number of bits grow large but is not an accurate approximation for low-resolution uniform quantizers.

A commonly adopted model for the error caused by a uniform quantizer is to approximate it as a noise term that is uncorrelated with the input and uniformly distributed in the interval $[-\Delta/2, \Delta/2]$, such that the PDF of e is (see, e.g., [65, Chapter 1.3], [66–69], and [70, Chapter 4.8])

$$f_e(e) \approx \begin{cases} \frac{1}{\Delta}, & -\frac{\Delta}{2} < e < \frac{\Delta}{2} \\ 0, & \text{otherwise.} \end{cases} \tag{3.6}$$

This approximation is sometimes called the pseudo-quantization noise (PQN) model [71]. Let $\sigma_y^2 = \mathbb{E}_y[y^2]$ and $\sigma_e^2 = \mathbb{E}_e[e^2]$ denote the variance of the input and the quantization error, respectively. Note that MSE $= \sigma_e^2$ for zero-mean inputs. Furthermore, let $\rho_{ye} = \mathbb{E}_y[ye]/(\sigma_y \sigma_e)$ denote the correlation between the input and the quantization error. According to the PQN model, it holds that $\sigma_e^2 \approx \frac{1}{\Delta} \int_{-\Delta/2}^{\Delta/2} e^2 \mathrm{d}e = \Delta^2/12$ and $\rho_{ye} \approx 0$. Next, we shall discuss the validity of the PQN model for the case of uniform quantization of Gaussian signals.

In Fig. 3.3, we compare the PDF of the quantization error e with the approximation (3.6) for $y \sim \mathcal{N}(0,1)$ and for MSE-optimal uniform quantizers with $Q \in \{1,2,3\}$ bits. We observe that the PQN model becomes increasingly accurate as the number of bits grow large. However, for low-resolution quantizers, there is a large discrepancy between the PDF according to the PQN model and the true PDF. In particular, we note that the quantization error is not contained within the interval $[-\Delta/2, \Delta/2]$ for Gaussian signals. Indeed, for finite-resolution quantizers, there will always be overload distortion for input signals that have infinite support.

(a) Variance of the quantization error as a function of the step size.

(b) Correlation between the input and the quantization error as a function of the step size.
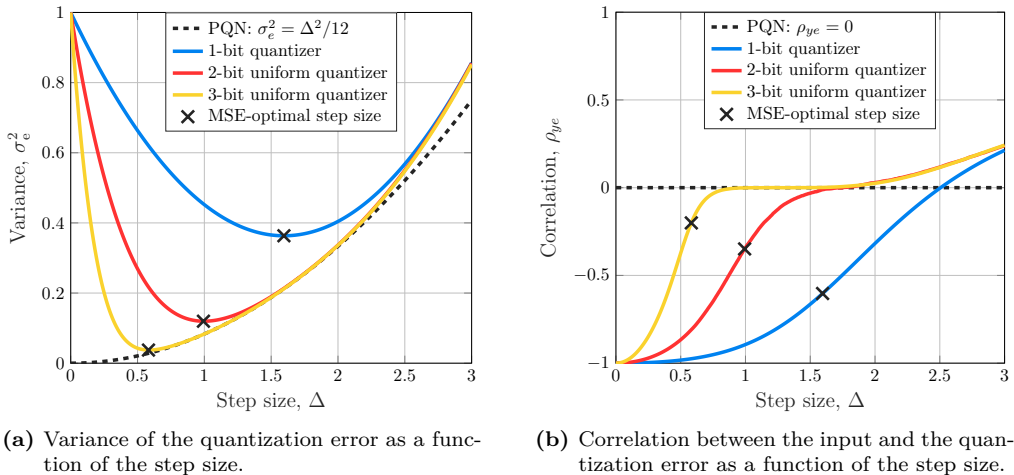
Figure 3.4: Variance of the quantization error and correlation between the input and the quantization error for a uniform quantizers and a $\mathcal{N}(0,1)$-distributed input. The PQN model becomes increasingly accurate as the number of bits grow large but is not an accurate approximation for low-resolution uniform quantizers.

In Fig. 3.4, we show the variance σ_e^2 and the correlation ρ_{ye} as a function the step size Δ for $y \sim \mathcal{N}(0,1)$ and for uniform quantizers with $Q \in \{1,2,3\}$ bits. Also shown are the approximations $\sigma_e^2 \approx \Delta^2/12$ and $\rho_{ye} \approx 0$ according to the PQN model We start by noting from Fig. 3.4a that, for 1-bit quantization, the PQN model significantly underestimates the variance of the quantization error. We further note from Fig. 3.4b that quantization error is, in general, correlated with the input signal. In particular, if the step size is set to minimize the MSE, there is a nonzero correlation between the input and the quantization error.

We conclude from Fig. 3.3 and Fig. 3.4 that the widely-adopted PQN model is not a suitable approximation for the quantization error caused by low-resolution (e.g., 1–3 bits) quantizers fed by Gaussian-distributed signals.

So far, we have only considered quantization of real-valued signals. For complex-valued signals $y \in \mathbb{C}$, it is commonly assumed that the real and imaginary components of the input are quantized independently. In this case, the quantized signal can be written as

$$r = \mathcal{Q}_\mathbb{C}(y) \tag{3.7}$$

where

$$\mathcal{Q}_\mathbb{C}(y) = \mathcal{Q}_\mathbb{R}(\Re\{y\}) + j\mathcal{Q}_\mathbb{R}(\Im\{y\}) \tag{3.8}$$

denotes the complex-valued quantization function.

Figure 3.5: Block diagram of the basic functions of an ADC [65, Fig. 1.1a].

3.2 Analog-to-Digital Converters

A block diagram of the basic functions of an ADC is shown in Fig. 3.5. The process of converting a continuous-time signal into a discrete-time signal is known as *sampling*. Let f_{samp} denote the sampling rate of the ADC, which is measured in samples per second (SPS). To ensure that the input to the sampling circuit adheres (at least approximately) to the sampling theorem, the analog input signal is passed through an anti-aliasing filter (a low-pass filter) prior to the sampling circuit. Throughout this thesis, we shall assume that the anti-aliasing filter is an ideal low-pass filter with a cut-off frequency f_{cut} that equals half the the sampling rate, i.e., $f_{\text{cut}} = f_{\text{samp}}/2$ such that any out-of-band (OOB) interference present in the analog input does not enter into the sampling circuit. We shall also assume that the sampling circuit is ideal (i.e., that there is no sampling-time jitter).

The discrete-time, continuous-amplitude output of the sampling circuit is fed to Q-bit quantizer, where Q is the resolution of the ADC (i.e., the number of ADC bits). While the sampling operation incurs no loss of information for band-limited signals. we recall from Sec. 3.1 that the nonlinear mapping of a continuous-amplitude signal into a finite set of possible labels introduces an error between the input and output of the quantizer, which can be made smaller by increasing the resolution of the ADC.

In an ideal ADC, the quantizer is the only source of distortion. Real-world ADCs, however, introduce additional noise and distortion caused by, for example, sampling-time jitter, integral nonlinearity, differential nonlinearity, and thermal noise [72, Chapter 6]. The effective number of bits (ENOB), which is defined as [65, Eq. (2.6)]

$$\text{ENOB} = \frac{\text{SNDR [dB]} - 1.76}{6.02} \tag{3.9}$$

is a widely used performance measure for real-world ADCs. Here, SNDR is the signal-to-noise-and-distortion ratio (SNDR), which is defined as the root-mean-square of the input to the ADC divided by the power of the noise and distortion terms that are present in the output of the ADC. Some comments on (3.9) are in order. For the case when an ideal Q-bit uniform quantizer is fed by a full-scale sinusoidal input $\gamma \sin(2\pi f t + \phi)$, where γ is the clipping level of the quantizer, by using the PQN approximation (3.6), the SNDR

can be approximated as follows:

$$\text{SNDR [dB]} \approx 10 \log_{10}\left(\frac{12\gamma^2 f}{\Delta^2} \int_0^{1/f} \sin^2(2\pi f t + \phi)\mathrm{d}t\right) \tag{3.10}$$

$$= 10 \log_{10}\left(\frac{6\gamma^2}{\Delta^2}\right) \tag{3.11}$$

$$\approx 6.02\,Q + 1.76. \tag{3.12}$$

Here, in the last step, we used that $\gamma = \Delta 2^{Q-1}$. By inserting (3.12) into (3.9), we get that $\text{ENOB} \approx Q$. Hence, in an ideal ADC, the ENOB is approximately equal to the number of bits. For real-world ADCs that introduce additional noise and distortion, the ENOB is typically a few bits (e.g., 1–3 bits) below the specified resolution (see, e.g., [73, Fig. 4]). According to (3.9), increasing the resolution of an ADC by one bit improves the SNDR by approximately 6 dB (a similar conclusion can be drawn from Fig. 3.2). Unfortunately, as we shall see next, increasing the resolution of an ADC also increases its power consumption.

A commonly used figure of merit (FOM) that relates the resolution and sampling rate of an ADC to the power consumption is the so-called Walden's FOM [73], which is based on empirical observations and is defined as follows [74, Eq. (1)]:

$$\text{FOM}_\text{W} = \frac{P_\text{diss}}{2^\text{ENOB} f_\text{snyq}}. \tag{3.13}$$

Here, P_diss is the power dissipation of the ADC and $f_\text{snyq} = f_\text{samp}/\text{OSR}$ is the Nyquist sample rate, where OSR is the oversampling ratio (OSR). Walden's FOM suggests that the power consumption scales linearly with the conversion rate. Furthermore, it suggests that increasing the resolution by one extra bit *doubles* the power consumption.

Another commonly used FOM is the so-called Schreier's FOM [75, Chapter 9], which is defined as follows [76, Eq. (13)]:

$$\text{FOM}_\text{S} \text{ [dB]} = \text{SNDR [dB]} + 10 \log_{10}\left(\frac{f_\text{snyq}}{2P_\text{diss}}\right) \tag{3.14}$$

$$\approx 6.02\,\text{ENOB} + 1.76 + 10 \log_{10}\left(\frac{f_\text{snyq}}{2P_\text{diss}}\right). \tag{3.15}$$

Similarly to Walden's FOM, Schreier's FOM suggests that the power consumption scales linearly with the conversion rate. However, differently from Walden's FOM, it suggests that increasing the resolution by extra one bit *quadruples* the power consumption.

In Fig. 3.6, we use the data collected in [77] to plot Walden's FOM (Fig. 3.6a) and Schreier's FOM (Fig. 3.6b), as a function of the Nyquist sampling rate, for real-world ADC designs presented at the International Solid-State Circuit Conference (ISSCC) and at the very-large-scale integration (VLSI) circuit symposium from 1997 to 2019. Fur-
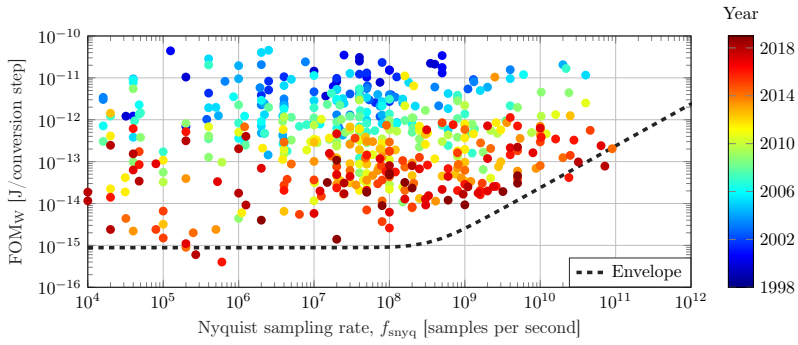
(a) Walden's FOM.
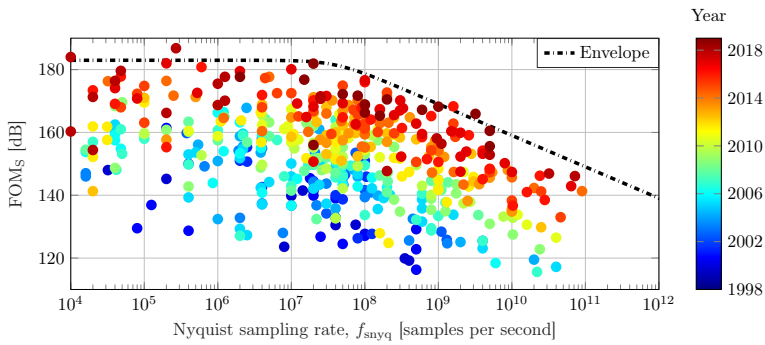
(b) Schreier's FOM.

Figure 3.6: Walden's FOM and Schreier's FOM as a function of the Nyquist data rate for ADC designs presented at ISSCC and at the VLSI circuit symposium [74]. The envelope lines are constructed from the 5–10 best designs as described in [74].
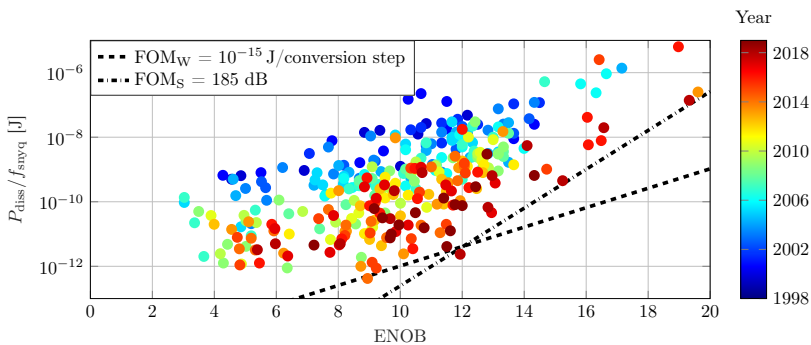
Figure 3.7: Energy ($P_{\text{diss}}/f_{\text{snyq}}$) versus ENOB for ADC designs presented at ISSCC and at the VLSI circuit symposium [74]
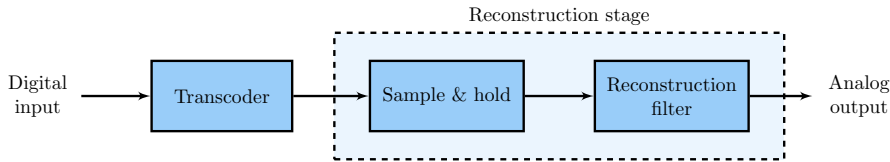
Figure 3.8: Block diagram of the basic functions of a DAC [65, Fig. 1.1b].

thermore, in Fig. 3.7, we plot the ratio $P_{\mathrm{diss}}/f_{\mathrm{snyq}}$ as the function of the ENOB. For reference, we also show the ratio $P_{\mathrm{diss}}/f_{\mathrm{snyq}}$ obtained from (3.13) by inserting $\mathrm{FOM}_W = 10^{-15}\,\mathrm{J/conversion}$ step and from (3.15) by inserting $\mathrm{FOM}_S = 185\,\mathrm{dB}$. We observe from Fig. 3.7 that Schreier's FOM, which predicts that $P_{\mathrm{diss}} \propto 4^{\mathrm{ENOB}}$, is a suitable metric for high-resolution ADCs (e.g., for ENOB > 11 bits) whereas Walden's FOM, which predicts that $P_{\mathrm{diss}} \propto 2^{\mathrm{ENOB}}$, is more suitable for low-to-moderate-resolution ADCs. In short, we conclude from Fig. 3.6 and Fig. 3.7 that the power consumption of an ADC increases *exponentially* with the the (effective) number of bits.

We further note from Fig. 3.6 that the power consumption increases super-linearly with the Nyquist sampling rate for high-speed ADCs (e.g., for $f_{\mathrm{snyq}} > 100\,\mathrm{MHz}$). This suggests that using low-resolution ADCs becomes a necessity for enabling efficient high-speed communication over the large bandwidths available in the millimeter-wave part of the radio spectrum.

In traditional MIMO systems, each RF port is connected to a pair of high-resolution and, hence, power-hungry ADCs. For example, a commercial 500 MSPS 16-bit ADC with 11.2 ENOB from Texas Instruments consumes 915 mW [78]. Using such high-resolution ADCs in a massive MU-MIMO system, where the number of antennas (and, hence, the number of ADCs) are in the order of hundreds, would lead to excessively high power consumption. Therefore, the resolution per BS-side ADC must be kept low in the massive MU-MIMO uplink to maintain a reasonable power budget.

3.3 Digital-to-Analog Converters

A block diagram of the basic functions of a DAC is shown in Fig. 3.8. According to this model, a DAC consists of a transcoder followed by a reconstruction stage. The transcoder produces an analog sequence whose amplitude is the analog representation of a digital code. The number of discrete amplitude levels in the transcoder output is determined by the resolution of the DAC (i.e., the number of DAC bits). In this thesis, it is assumed that the DSP unit uses floating-point arithmetic with infinite word length. The transcoder in a Q-bit DAC, which supports only 2^Q voltage levels, can therefore be modeled as a Q-bit quantizer.

The reconstruction stage transforms the transcoder output into an analog waveform. Typically, this block consists of a sample-and-hold circuit followed by a low-pass filter.

Note that the sample-and-hold circuit and the transcoder are often implemented in the same circuit [65, Chapter 1.7]. A common sample-and-hold circuit is a zero-order hold (ZOH) filter, which holds the amplitude of the each sample for a prescribed time duration. Unfortunately, a ZOH filter has a frequency response with infinite support, which causes unwanted OOB emissions. To reduce these OOB emissions, a low-pass filter is installed after the sample-and-hold circuit. In this thesis, we will assume that the reconstruction stage is an ideal low-pass filter with cut-off frequency $f_{\mathrm{cut}} = f_{\mathrm{samp}}/2$.

DACs typically consume less power than ADCs [35]. For reference, a commercial 500 MSPS 14-bit DAC from Texas Instruments consume 375 mW [79]. However, significantly more energy-efficient designs have been reported in the academic literature (see, e.g., [80–82]). Nevertheless, as is the case with ADCs, using DACs with unnecessarily high resolution will result in excessive power consumption, which motivates the use of low-resolution DACs in the massive MU-MIMO downlink.

Taming Nonlinearities using Bussgang's Theorem

Nonlinearities are ubiquitous in virtually all real-world information-processing systems. For example, analog RF signals in wireless communication systems are typically passed through amplifiers, mixers, and finite-resolution data converters. All of these devices are nonlinear and will, to some extent, distort the signals of interest. However, an exact performance analysis of nonlinear systems and recovering signals from nonlinear measurements are generally difficult tasks. Therefore, despite their prevalence in real-world systems, the impact of nonlinearities is routinely ignored or approximated using simplified models whose accuracy is questionable. For example, we saw in Sec. 3.1 that the widely-used PQN model does not provide a sufficiently accurate approximation for the error introduced by low-resolution quantization of Gaussian signals. In this chapter, we shall "tame" nonlinearities using *Bussgang's theorem* [83] and derive lower bound on the rate achievable in communication systems subject to nonlinear distortion.

4.1 Linearization using LMMSE Estimation

Consider a zero-mean random vector $\mathbf{y} \in \mathbb{C}^M$ being passed through some scalar-valued nonlinear function $f(\,\cdot\,) : \mathbb{C} \to \mathbb{C}$, which is applied element-wise to the vector, to produce the following output:

$$\mathbf{r} = f(\mathbf{y}). \tag{4.1}$$

The LMMSE estimate of the nonlinearly-distorted signal $\mathbf{r} \in \mathbb{C}^M$ in (4.1) given the input $\mathbf{y}$ can be written as $\mathbf{G}^{\mathrm{est}}\mathbf{y}$, where $\mathbf{G}^{\mathrm{est}} \in \mathbb{C}^{M \times M}$ is the solution to the following

optimization problem:

$$\mathbf{G}^{\text{est}} = \underset{\widetilde{\mathbf{G}} \in \mathbb{C}^{M \times M}}{\operatorname{argmin}} \; \mathbb{E}_{\mathbf{y}}\Big[\|\mathbf{r} - \widetilde{\mathbf{G}}\mathbf{y}\|_2^2\Big]. \tag{4.2}$$

In words, solving the above optimization problem yields the matrix $\mathbf{G}^{\text{est}}$ that minimizes the MSE between the linear estimator and the nonlinearly distorted output. The MSE-optimal matrix $\mathbf{G}^{\text{est}}$ is found by setting the gradient of (4.2) to zero, which yields

$$\mathbf{G}^{\text{est}} = \mathbf{C_{ry}}\mathbf{C_y}^{-1} \tag{4.3}$$

where $\mathbf{C_{ry}} = \mathbb{E}\big[\mathbf{r}\mathbf{y}^H\big] \in \mathbb{C}^{M \times M}$ is the cross-covariance of $\mathbf{r}$ and $\mathbf{y}$, and $\mathbf{C_y} = \mathbb{E}\big[\mathbf{y}\mathbf{y}^H\big] \in \mathbb{C}^{M \times M}$ is the covariance $\mathbf{y}$. It follows from (4.3) that the nonlinearly distorted signal $\mathbf{r}$ in (4.1) can be written as

$$\mathbf{r} = \mathbf{G}^{\text{est}}\mathbf{y} + \mathbf{e} \tag{4.4}$$

where the distortion term $\mathbf{e} \in \mathbb{C}^M$ is *uncorrelated* with the input $\mathbf{y}$. Indeed,

$$\mathbb{E}\big[\mathbf{e}\mathbf{y}^H\big] = \mathbb{E}\big[\big(\mathbf{r} - \mathbf{G}^{\text{est}}\mathbf{y}\big)\mathbf{y}^H\big] = \mathbf{C_{ry}} - \mathbf{G}^{\text{est}}\mathbf{C_y} = \mathbf{C_{ry}} - \mathbf{C_{ry}}\mathbf{C_y}^{-1}\mathbf{C_y} = \mathbf{0}_{M \times M}. \tag{4.5}$$

Note that (4.4) provides a linear relationship between the input and output of the nonlinear device. However, deriving an expression for the matrix $\mathbf{G}^{\text{est}}$ in (4.3) involves computing the inverse of the $M \times M$ covariance matrix $\mathbf{C_y}$, which is tedious for large M and requires $\mathbf{C_y}$ to be invertible. Furthermore, the cross-covariance matrix $\mathbf{C_{ry}}$ is not always available in closed form. Next, we shall consider a special case of (4.4) for which computing $\mathbf{G}^{\text{est}}$ can be significantly simplified.

4.2 Linearization using Bussgang's Theorem

Bussgang wrote in 1952 that [83]: "*For two Gaussian signals, the cross-correlation function taken after one of them has undergone nonlinear amplitude distortion is identical, except for a factor of proportionality, to the cross-correlation function taken before the distortion.*" Concretely, according to Bussgang's theorem, for a pair of zero-mean jointly complex Gaussian random variables $y_m \sim \mathcal{CN}(0, \sigma_{y_m}^2)$ and $y_n \sim \mathcal{CN}(0, \sigma_{y_n}^2)$, and for $r_m = f(y_m)$, it holds that [83–85]

$$\mathbb{E}_{r_m,y_n}[r_m y_n^*] = g_m \, \mathbb{E}_{y_m,y_n}[y_m y_n^*] \tag{4.6}$$

where

$$g_m = \frac{1}{\sigma_{y_m}^2} \, \mathbb{E}_{y_m}[f(y_m)y_m^*]. \tag{4.7}$$

For a zero-mean complex Gaussian random vector $\mathbf{y} = [y_1, y_2, \ldots, y_M] \sim \mathcal{CN}(\mathbf{0}_{M \times 1}, \mathbf{C_y})$ and for $\mathbf{r} = f(\mathbf{y})$, it follows from (4.6) that

$$\mathbf{C_{ry}} = \mathbf{G C_y} \tag{4.8}$$

where

$$\mathbf{G} = \text{diag}\left([g_1, g_2, \ldots, g_M]^T\right) \tag{4.9}$$

is a *diagonal $M \times M$* matrix whose mth diagonal entry is computed as in (4.7).

Bussgang's theorem can be used to decompose the output of a nonlinear device as a linear function of the input $\mathbf{y}$ and a distortion $\mathbf{d} \in \mathbb{C}^M$ that is uncorrelated (but not independent) with the input in the following manner [86]:

$$\mathbf{r} = \mathbf{G y} + \mathbf{d}. \tag{4.10}$$

Indeed,

$$\mathbb{E}\left[\mathbf{d y}^H\right] = \mathbb{E}\left[(\mathbf{r} - \mathbf{G y})\,\mathbf{y}^H\right] = \mathbf{C_{ry}} - \mathbf{G C_y} = \mathbf{0}_{M \times M} \tag{4.11}$$

where the last equality holds because $\mathbf{C_{ry}} = \mathbf{G C_y}$.

Note that (4.10), similarly to the LMMSE decomposition in (4.4), provides a linear relationship between the input and output of a nonlinear device. It turns out that the diagonal Bussgang gain matrix $\mathbf{G}$ in (4.9) can be computed in closed form for a broad range of nonlinearities, which often simplifies performance analyses. Bussgang's theorem has therefore found widespread use as a tool for evaluating the impact on performance of nonlinear distortion in wireless communication systems (see, e.g., [87–91]) and in the development of distortion-aware signal-processing algorithms (see, e.g., [92–94]). It has also found application in several other areas including probit regression [95], phase retrieval [96], and satellite positioning [97].

4.3 A Lower Bound on Channel Capacity

The linear decomposition in (4.10) makes it possible to derive a lower bound on the channel capacity in communication systems that suffer from nonlinear distortion. In this section, the details of said derivation is provided for a single-input single-output channel subject to nonlinear distortion in the form of coarse output quantization. Specifically, in this section, we shall consider the following channel:

$$r = \mathcal{Q}_{\mathbb{C}}(y) = \mathcal{Q}_{\mathbb{C}}(x + w). \tag{4.12}$$

Here, $x \in \mathbb{C}$ is the channel input and $w \sim \mathcal{CN}(0, N_0)$ is the AWGN. Furthermore, $\mathcal{Q}_{\mathbb{C}}(\,\cdot\,) : \mathbb{C} \to \mathcal{L} \times \mathcal{L}$ is the complex-valued quantization function defined in (3.8), where

$\mathcal{L}$ is the set of quantization labels For a fixed quantizer, the capacity of the channel (4.12) is [98, Eq. (4)]

$$C = \sup_{f_x} \ \mathcal{I}(x; r) \tag{4.13}$$

where the supremum is over all probability distributions f_x for which the average power constraint $\mathbb{E}_x\big[|x|^2\big] < P_x$ is satisfied. The channel capacity in (4.13) is, in general, not available in closed form due to the nonlinearity in the quantizer. In what follows, we shall utilize Bussgang's theorem to derive a lower bound on the rate achievable with Gaussian signaling. To this end, by assuming that $x \sim \mathcal{CN}(0, P_x)$, we decompose the quantized channel input-output model in (4.12) using Bussgang's theorem as follows:

$$r = gx + gw + d. \tag{4.14}$$

Here, the distortion term d, unlike the quantization error in (3.5), is uncorrelated with y (and also with x and w) and

$$g = \frac{1}{P_x + N_0} \ \mathbb{E}[\mathcal{Q}_{\mathbb{C}}(y)y^*]. \tag{4.15}$$

Closed-form expressions for the gain in (4.15) are provided in [99, Eq. (29)] and [100, Eq. (11)] for the case of uniform and nonuniform quantization, respectively. From the linearized channel input-output model (4.14), it becomes straightforward to separate the desired and undesired signal components. The first term on the RHS of (4.14) corresponds to the desired signal; the second term correspond to the AWGN; the third term correspond to the distortion caused by the finite-resolution quantizer. The effective SNDR at the receiver can, hence, be expressed as follows:

$$\text{SNDR} = \frac{g^2 P_x}{g^2 N_0 + P_d}. \tag{4.16}$$

Here, $P_d = \mathbb{E}_d\big[|d|^2\big]$. Since y and d are uncorrelated, it follows from (4.14) that

$$P_d = P_r - g^2 P_x - g^2 N_0. \tag{4.17}$$

where $P_r = \mathbb{E}_r\big[|r|^2\big]$. It is worth emphasizing at this point that the effective noise $gw+d$ in the linearized channel input-output model (4.14) is, in general, non-Gaussian distributed due to the nonlinearity in the quantizer, which complicates an exact evaluation of the achievable rate. A common approach is to make use of the so-called "auxiliary-channel lower bound" (see, e.g., [101, Sec. VI]) to derive a lower bound on the achievable rate. Specifically, consider the the auxiliary channel

$$\tilde{r} = gx + \tilde{w} \tag{4.18}$$

where $\tilde{w} \sim \mathcal{CN}(0, g^2 N_0 + P_d)$ is the auxiliary noise, which has the same variance as the effective noise $gw + d$ but is Gaussian distributed. A lower bound on the channel capacity C in (4.13) is obtained through the following steps:

$$C \geq \mathcal{I}(x; r) \tag{4.19}$$

$$= \mathbb{E}_{x,r}\left[\log_2\left(\frac{f_{x,r}(x, r)}{f_x(x) f_r(r)}\right)\right] \tag{4.20}$$

$$= \mathbb{E}_{x,r}\left[\log_2\left(\frac{f_{x,\tilde{r}}(x, r)}{f_x(x) f_{\tilde{r}}(r)}\right)\right] + \mathbb{E}_{x,r}\left[\log_2\left(\frac{f_{x,r}(x, r)}{f_{x|\tilde{r}}(x|r) f_r(r)}\right)\right] \tag{4.21}$$

$$= \mathbb{E}_{x,r}\left[\log_2\left(\frac{f_{x,\tilde{r}}(x, r)}{f_x(x) f_{\tilde{r}}(r)}\right)\right] + \mathcal{D}(f_{x,r} || f_{x|\tilde{r}} f_r) \tag{4.22}$$

$$\geq R. \tag{4.23}$$

Here, in the last step, we have defined $R = \mathbb{E}_{x,r}[\log_2(f_{x,\tilde{r}}(x, r)/(f_x(x) f_{\tilde{r}}(r)))]$. The inequality (4.19) holds as we have restricted the input to follow a Gaussian distribution. The inequality (4.23) holds due to the nonnegativity of Kullback-Leibler divergence [102, Thm. 8.6.3]. This inequality holds with equality if and only if $\tilde{r} = r$ (i.e., if and only if $\tilde{w} = gw + d$). For the auxiliary channel (4.18), it holds that

$$f_{\tilde{r}|x}(r|x) = \frac{1}{\pi(g^2 N_0 + P_d)} \exp\left(-\frac{|r - gx|^2}{g^2 N_0 + P_d}\right) \tag{4.24}$$

and

$$f_{\tilde{r}}(r) = \frac{1}{\pi P_r} \exp\left(-\frac{|r|^2}{P_r}\right). \tag{4.25}$$

Hence, the rate R in (4.23) can be expanded as follows:

$$R = \mathbb{E}_{x,r}\left[\log_2\left(\frac{f_{x,\tilde{r}}(x, r)}{f_x(x) f_{\tilde{r}}(r)}\right)\right] \tag{4.26}$$

$$= \mathbb{E}_{x,r}\left[\log_2\left(\frac{f_{\tilde{r}|x}(r|x)}{f_{\tilde{r}}(r)}\right)\right] \tag{4.27}$$

$$= \mathbb{E}_{x,r}\left[\log_2\left(\frac{P_r}{g^2 N_0 + P_d} \exp\left(\frac{|r|^2}{P_r} - \frac{|r - gx|^2}{g^2 N_0 + P_d}\right)\right)\right] \tag{4.28}$$

$$= \log_2\left(\frac{P_r}{g^2 N_0 + P_d}\right) + \frac{1}{P_r} \mathbb{E}_{x,r}\left[|r|^2\right] - \frac{1}{g^2 N_0 + P_d} \mathbb{E}_{w,d}\left[|gw + d|^2\right] \tag{4.29}$$

$$= \log_2(1 + \text{SNDR}). \tag{4.30}$$

Here, in the last step, we used that $P_r = g^2 P_x + g^2 N_0 + P_d$ (see (4.17)).

The rate in (4.30) provides a lower bound in closed form on the capacity of the

nonlinearly-distorted channel (4.12). It can be shown that this lower bound corresponds to the rate achieved by a Gaussian codebook and mismatched scaled nearest-neighbor decoding at the receiver [88, 103].

Next, we evaluate the lower bound (4.30) for the case of 1-bit quantization. For $\mathcal{L} = \{-1/\sqrt{2},\ 1/\sqrt{2}\}$ (or, equivalently, for $\Delta = \sqrt{2}$ and $Q = 1$), the complex-valued quantization function in (3.8) simplifies to

$$\mathcal{Q}_{\mathbb{C}}(y) = \sqrt{\frac{1}{2}}\Big(\operatorname{sgn}(\Re\{y\}) + j\operatorname{sgn}(\Im\{y\})\Big). \tag{4.31}$$

Note that, with these choices, it holds that $r \in \sqrt{1/2}\,\{1+j, -1+j, -1-j, 1-j\}$ and that $P_r = 1$. By inserting (4.31) into (4.15), we get that

$$g = \sqrt{\frac{2}{\pi(P_x + N_0)}}. \tag{4.32}$$

Furthermore, by inserting (4.32) into (4.33), we find that the effective SNDR after 1-bit quantization is

$$\text{SNDR} = \frac{(2/\pi)\,P_x}{N_0 + (1 - 2/\pi)P_x} = \frac{(2/\pi)\,\text{SNR}}{1 + (1 - 2/\pi)\,\text{SNR}} \tag{4.33}$$

where $\text{SNR} = P_x/N_0$. Hence,

$$R = \log_2\left(1 + \frac{(2/\pi)\,\text{SNR}}{1 + (1 - 2/\pi)\,\text{SNR}}\right). \tag{4.34}$$

For the case of 1-bit quantization, it is well-known that the channel capacity in (4.13) is achieved by quadrature phase-shift keying (QPSK) signaling and is given by (see, e.g., [104, Thm. 2])

$$C = 2\Big(1 - \mathcal{H}\Big(\Phi\Big(\sqrt{\text{SNR}}\Big)\Big)\Big). \tag{4.35}$$

In the low-SNR regime, the channel capacity (4.35) converges to a factor $2/\pi$ of the AWGN channel capacity $\log_2(1 + \text{SNR})$ [105, Eq. (3.4.20)] (see also [98, Sec. II]), which corresponds to a $10\log_{10}(2/\pi) \approx 2\,\text{dB}$ power loss due to 1-bit quantization. This holds true also for the lower bound in (4.34). Indeed, $\lim_{\text{SNR}\to 0} R/\log_2(1 + \text{SNR}) = 2/\pi$. In the high-SNR regime, on the other hand, the lower bound (4.34) converges to a factor $\lim_{\text{SNR}\to\infty} = R/C = \log_2(\pi/(\pi - 2))/2 \approx 0.73$ of the channel capacity (4.35).

Fig. 4.1 shows the achievable rate (4.34) and the channel capacity (4.35) as a function of the SNR. For reference, the AWGN channel capacity $\log_2(1 + \text{SNR})$ is also shown. As expected, we note that the lower bound is tight in the low-SNR regime but that there is a significant gap in the high-SNR regime.

For the case of multi-bit quantization (i.e., for $Q > 1$), the channel capacity (4.13) is not
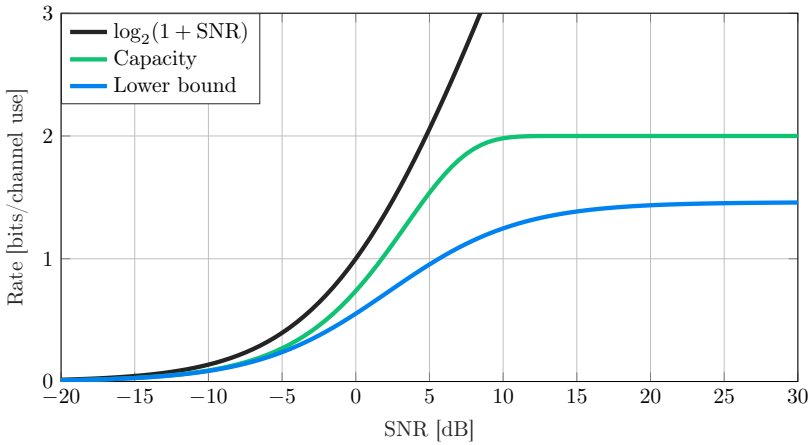
Figure 4.1: Comparison of channel capacity (4.35) and the rate achievable with Gaussian inputs (4.34) for the case of 1-bit quantization.

available in closed form. In this case, (4.30) provides a useful lower bound on the capacity of the quantized channel (4.12). For example, for the case of uniform quantization, the gain in (4.15) is given by [99, Eq. (29)]

$$g = \frac{\Delta}{\sqrt{\pi(P_x + N_0)}} \sum_{q=1}^{2^Q-1} \exp\left(-\frac{\Delta^2(q - 2^{Q-1})^2}{P_x + N_0}\right). \tag{4.36}$$

Furthermore, it can be shown that

$$\begin{aligned} P_d = {}& \frac{\Delta^2}{2}(2^Q - 1)^2 - g^2(P_x + N_0) \\ & -4\Delta^2 \sum_{q=1}^{2^Q-1} (q - 2^{Q-1}) \, \Phi\left(\frac{\sqrt{2}\Delta(q - 2^{Q-1})}{\sqrt{P_x + N_0}}\right). \end{aligned} \tag{4.37}$$

Hence, by inserting (4.36), (4.37), and (4.16) into (4.30) we obtain a closed-form lower bound on the channel capacity in (4.13). Fig. 4.2 depicts this lower bound for uniform quantization with $Q \in \{1, 2, \ldots, 6\}$ bits. Here, the step size Δ is set to minimize the MSE of the quantization error in (3.5) for each value of SNR. We note that $Q = 6$ bits is sufficient for closing the gap to the AWGN channel capacity (which serves as an upper bound on the channel capacity (4.13) and, hence, on the rate (4.30)) for SNR < 20 dB.

To summarize, in this chapter, Bussgang's theorem has been utilized to write the output of a nonlinear device, which is fed by Gaussian inputs, as a linear function of the input and an uncorrelated distortion term. This representation is convenient as it allows us to develop lower bounds on the achievable rate in systems that suffer from nonlinear
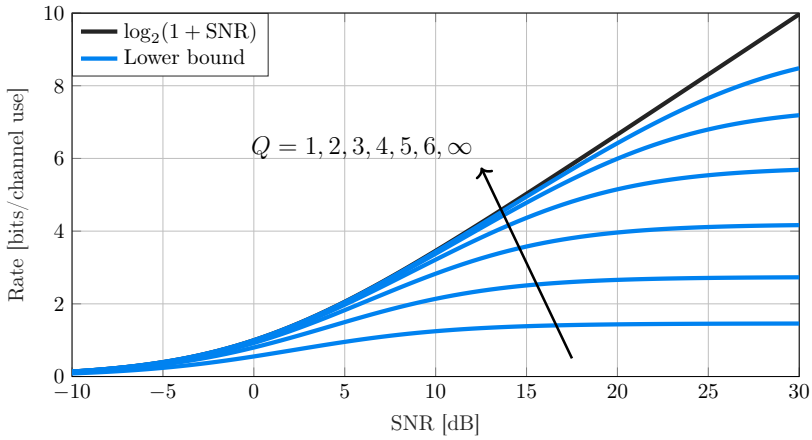
Figure 4.2: Lower bound on the rate achievable with Gaussian inputs (4.34) for MSE-optimal uniform quantization with $Q \in \{1, 2, \ldots, 6\}$ bits. As the number of bits increases, the rate (4.34) approaches the AWGN channel capacity.

distortion. Furthermore, such lower bounds provide an accurate approximation for the rate achievable with orthogonal frequency-division multiplexing (OFDM) modulation, used frequently in real-world systems (e.g., in LTE and NR [5,19]), for which the transmit waveform can be accurately approximated as a Gaussian random process.

Massive MU-MIMO with Low-Resolution Data Converters

This chapter introduces the massive MU-MIMO system model for that case when the BS is equipped with low-resolution data converters. Specifically, Sec. 5.1 provides an introduction to the massive MU-MIMO uplink with low-resolution ADCs at the BS. An introduction to the massive MU-MIMO downlink with low-resolution DACs at the BS is provided in Sec. 5.2.

Recall from Chapter 3 that the power consumption of a data converter is reduced by lowering its resolution. There may also be some secondary power-saving effects as the use of low-resolution data converters could simplify the analog front end. For example, in a 1-bit-ADC architecture, there may be no need for any automatic gain control circuitry, which is typically required for adjusting the amplitude of the received signal to the dynamic range (i.e., to the clipping level) of the ADC. Furthermore, using low-resolution DACs to generate the transmit waveform in the massive MU-MIMO downlink reduces the per-antenna peak-to-average power ratio (PAPR) [106], which, in turn, allows for power-efficient PA designs [107].

Another motivation for reducing the resolution of the data converters is to limit the excessively large amount of data that must be transferred over the interface connecting the DSP unit to the data converters [108,109]. This becomes critical for systems operating over large bandwidths in the millimeter-wave part of the wireless spectrum [17], and for distributed architectures (e.g., cell-free massive MU-MIMO systems [110] and cloud radio access networks [111,112]) where the data converters may be placed at a significant distance from the DSP unit. Consider, for example, using a pair of 500 MSPS 16-bit ADCs (e.g., the ADC from Texas Instruments in [78]) at each antenna element in a BS that is equipped with 64 active antenna elements. For such a system, the combined

amount of data produced by the ADCs is more than 1 Tbit/s, which exceeds by far the rates supported by modern high-speed interconnects such as JESD204B [113] and the (evolved) common public radio interface (CPRI) [114]. By lowering the resolution of the data converters, one can, to some extent, mitigate this data rate bottleneck.

5.1 Massive MU-MIMO with Low-Resolution ADCs

We consider a single-cell massive MU-MIMO uplink system where U single-antenna UEs transmit simultaneously to a B-antenna BS. In what follows, we shall assume that all BS-side hardware components (e.g., LNAs, LOs, and mixers) except for the ADCs are ideal. We further assume perfect timing and frequency synchronization between the BS and the UEs. Indeed, it has been shown in, e.g., [115–119] that accurate timing and frequency synchronization can be achieved even under coarse quantization. Finally, for simplicity, we shall assume that the system operates over a frequency-flat channel. With these assumptions and for the ADC model introduced in Sec. 3.2, the signal received at the BS during the uplink phase can be written as follows:

$$\mathbf{r}^{\mathrm{ul}}[n] = \mathcal{Q}_{\mathbb{C}}\big(\mathbf{y}^{\mathrm{ul}}[n]\big) = \mathcal{Q}_{\mathbb{C}}\big(\mathbf{H}\mathbf{s}^{\mathrm{ul}}[n] + \mathbf{w}^{\mathrm{ul}}[n]\big). \tag{5.1}$$

Here, $\mathcal{Q}_{\mathbb{C}}(\,\cdot\,) : \mathbb{C} \to \mathcal{L} \times \mathcal{L}$ is the complex-valued quantization function defined in (3.8), where $\mathcal{L}$ is the set of quantization labels. Furthermore, as in Sec. 2.2, $\mathbf{s}^{\mathrm{ul}}[n] \in \mathbb{C}^U$ are the transmitted symbols from the U UEs, for which it holds that $\mathbb{E}\big[\mathbf{s}^{\mathrm{ul}}[n](\mathbf{s}^{\mathrm{ul}}[n])^H\big] \leq P^{\mathrm{ul}}\mathbf{I}_U$. Finally, $\mathbf{w}^{\mathrm{ul}}[n] \sim \mathcal{CN}(\mathbf{0}_{B \times 1}, N_0^{\mathrm{ul}}\mathbf{I}_B)$ is the BS-side AWGN and $\mathbf{H} \in \mathbb{C}^{B \times U}$ is the channel matrix.

There have been a significant amount of works that consider the use of low-resolution ADCs in the massive MU-MIMO uplink (see, e.g., [120–135]). Broadly speaking, these works can be divided into two groups. The first group of works investigate the impact of low-resolution quantization on the performance of conventional linear receiver processing algorithms, which have low computational complexity and are known to yield near-optimal performance as the number of antennas grow large. The second group of works considers more sophisticated nonlinear receiver algorithms that explicitly take into account the impact of the coarse quantization to improve some performance metric at the cost of increased computational complexity.

In this thesis, we shall restrict our analysis to the case of linear receiver processing at the BS. In this scenario, Bussgang's theorem can be utilized for providing lower bounds on the rate achievable with Gaussian signaling. The remainder of this section outlines how the analysis in Chapter 4 can be extended to the low-resolution-quantized massive MU-MIMO uplink. To this end, by assuming perfect CSI at the BS and by proceeding as in Sec. 4.2, we decompose the quantized channel input-output model (5.1) for the case

of Gaussian inputs as

$$\mathbf{r}^{\mathrm{ul}}[n] = \mathbf{G}\mathbf{y}^{\mathrm{ul}}[n] + \mathbf{d}^{\mathrm{ul}}[n] = \mathbf{G}\mathbf{H}\mathbf{s}^{\mathrm{ul}}[n] + \mathbf{G}\mathbf{w}^{\mathrm{ul}}[n] + \mathbf{d}^{\mathrm{ul}}[n] \tag{5.2}$$

where the distortion term $\mathbf{d}^{\mathrm{ul}}[n] \in \mathbb{C}^B$ is uncorrelated with the transmitted symbols. Furthermore, $\mathbf{G}$ can be written as [100, Eq. (9)]

$$\begin{aligned}
\mathbf{G} = \operatorname{diag}\big(\mathbf{C}_{\mathbf{y}^{\mathrm{ul}}}\big)^{-1/2} \sum_{q=0}^{2^Q-1} \frac{\ell_q}{\sqrt{\pi}} \\
\times \Big(\exp\big(-\tau_q^2 \operatorname{diag}\big(\mathbf{C}_{\mathbf{y}^{\mathrm{ul}}}\big)^{-1}\big) - \exp\big(-\tau_{q+1}^2 \operatorname{diag}\big(\mathbf{C}_{\mathbf{y}^{\mathrm{ul}}}\big)^{-1}\big) \Big)
\end{aligned} \tag{5.3}$$

where $\mathbf{C}_{\mathbf{y}^{\mathrm{ul}}} = \mathbb{E}\big[\mathbf{y}^{\mathrm{ul}}[n](\mathbf{y}^{\mathrm{ul}}[n])^H\big] = P^{\mathrm{ul}}\mathbf{H}\mathbf{H}^H + N_0^{\mathrm{ul}}\mathbf{I}_B \in \mathbb{C}^{B \times B}$ is the covariance of $\mathbf{y}^{\mathrm{ul}}[n]$. Furthermore, as in Sec. 3.1, ℓ_q is the qth element of the set of quantization labels $\mathcal{L}$ and τ_q is the qth element of the set of quantization thresholds $\mathcal{T}$. For the case of uniform quantization, i.e., for $\ell_q = \Delta\big(q - 2^{Q-1} + 1/2\big)$ for $q = 0, 1, \ldots, 2^Q - 1$ and $\tau_q = \Delta\big(q - 2^{Q-1}\big)$ for $q = 1, 2, \ldots, 2^Q - 1$, (5.3) simplifies to [99, Eq. (14)]

$$\mathbf{G} = \frac{\Delta}{\sqrt{\pi}} \operatorname{diag}\big(\mathbf{C}_{\mathbf{y}^{\mathrm{ul}}}\big)^{-1/2} \sum_{q=1}^{2^Q-1} \exp\Big(-\Delta^2\big(q - 2^{Q-1}\big)^2 \operatorname{diag}\big(\mathbf{C}_{\mathbf{y}^{\mathrm{ul}}}\big)^{-1}\Big). \tag{5.4}$$

For the case of 1-bit quantization, (5.4) further simplifies to

$$\mathbf{G} = \frac{\Delta}{\sqrt{\pi}} \operatorname{diag}\big(\mathbf{C}_{\mathbf{y}^{\mathrm{ul}}}\big)^{-1/2}. \tag{5.5}$$

Note that (5.5) can be retrieved also from (5.3) as $\Delta = \ell_1 - \ell_0$ and $\mathcal{T} = \{-\infty, 0, \infty\}$ for the case $Q = 1$.

With linear combining and low-resolution ADCs at the BS, an estimate of the symbol transmitted from the uth UE is given by

$$z_u^{\mathrm{ul}}[n] = \mathbf{a}_u^T \mathbf{r}^{\mathrm{ul}}[n] = \mathbf{a}_u^T \mathbf{G}\mathbf{h}_u s_u^{\mathrm{ul}}[n] + \sum_{v \neq u} \mathbf{a}_u^T \mathbf{G}\mathbf{h}_v s_v^{\mathrm{ul}}[n] + \mathbf{a}_u^T \mathbf{G}\mathbf{w}^{\mathrm{ul}}[n] + \mathbf{a}_u^T \mathbf{d}^{\mathrm{ul}}[n] \tag{5.6}$$

for $u = 1, 2, \ldots, U$, Here, $\mathbf{a}_u \in \mathbb{C}^B$ is the uth column of the the combining matrix in (2.7). Note that (5.6) provides a linear relationship between the transmitted and received symbols. Hence, by proceeding analogously to Sec. 4.3, the sum rate achievable with Gaussian inputs can be lower bounded by

$$R^{\mathrm{ul}} = \mathbb{E}_{\mathbf{H}}\left[\sum_{u=1}^{U} \log_2\Big(1 + \mathrm{SINDR}_u^{\mathrm{ul}}\Big) \right] \tag{5.7}$$

where

$$\text{SINDR}_u^{\text{ul}} = \frac{P^{\text{ul}}\left|\mathbf{a}_u^T\mathbf{G}\mathbf{h}_u\right|^2}{P^{\text{ul}}\sum_{v\neq u}\left|\mathbf{a}_u^T\mathbf{G}\mathbf{h}_v\right|^2 + N_0^{\text{ul}}\|\mathbf{a}_u\mathbf{G}\|_2^2 + \mathbf{a}_u^T\mathbf{C}_{\mathbf{d}^{\text{ul}}}\mathbf{a}_u} \tag{5.8}$$

is the uplink signal-to-interference-noise-and-distortion ratio (SINDR) for the uth UE. Here, $\mathbf{C}_{\mathbf{d}^{\text{ul}}} = \mathbb{E}\left[\mathbf{d}^{\text{ul}}[n](\mathbf{d}^{\text{ul}}[n])^H\right] \in \mathbb{C}^{B\times B}$ is the covariance of $\mathbf{d}^{\text{ul}}[n]$. For the case of 1-bit quantization, the covariance matrix $\mathbf{C}_{\mathbf{d}^{\text{ul}}}$, which is required to evaluate (5.8), can be computed in closed form using Van Vleck's arcsine law [136]. For the multi-bit case, the covariance matrix $\mathbf{C}_{\mathbf{d}^{\text{ul}}}$ is not available in closed form and, hence, has to be evaluated numerically [137] or by using approximate models (see, e.g., [109, 138]).

5.2 Massive MU-MIMO with Low-Resolution DACs

We now turn our attention to the downlink scenario in which the B-antenna BS serves simultaneously the U single-antenna UEs. We again assume that all BS-side hardware components (e.g., PAs, LOs, and mixers) excepts for the DACs are ideal, that the system operates over a frequency-flat channel, and that it is perfectly synchronized. With these assumptions and for the DAC model introduced in Sec. 3.3, the signal received at the U UEs during the downlink phase can be written as follows:

$$\mathbf{y}^{\text{dl}}[n] = \mathbf{H}^T\mathbf{x}^{\text{dl}}[n] + \mathbf{w}^{\text{dl}}[n]. \tag{5.9}$$

Here, as in Sec. 2.3, $\mathbf{w}^{\text{dl}}[n] \sim \mathcal{CN}(\mathbf{0}_{U\times 1}, N_0^{\text{dl}}\mathbf{I}_U)$ is the UE-side AWGN and $\mathbf{x}^{\text{dl}}[n]$ is the B-dimensional transmit signal for which it holds that $\mathbb{E}_{\mathbf{H}}\left[\|\mathbf{x}^{\text{dl}}[n]\|_2^2\right] \leq P^{\text{dl}}$. Due to the finite-resolution DACs, we additionally require that the transmitted vector satisfies $\mathbf{x}^{\text{dl}}[n] \in \mathcal{X}^B$, where $\mathcal{X} = \mathcal{L} \times \mathcal{L}$ is the set complex-valued DAC outputs supported at each antenna element.

In this thesis, we shall consider linear and nonlinear precoding schemes for the low-resolution-quantized massive MU-MIMO downlink. Linear precoding has been considered in, e.g., [93, 99, 109, 139, 140] and is known to yield good performance for large antenna arrays even in the presence of coarse quantization. With linear precoding, the transmitted vector in (5.9) can be written as follows:

$$\mathbf{x}^{\text{dl}}[n] = \mathcal{Q}_{\mathbb{C}}(\alpha\mathbf{P}\mathbf{s}^{\text{dl}}[n]). \tag{5.10}$$

Here, $\mathbf{P} \in \mathbb{C}^{B\times U}$ is the precoding matrix in (2.16) and $\mathbf{s}^{\text{dl}}[n] \in \mathbb{C}^U$ are symbols intended for the U UEs, for which it holds that $\mathbb{E}\left[\mathbf{s}^{\text{dl}}[n](\mathbf{s}^{\text{dl}}[n])^H\right] \leq P^{\text{dl}}\mathbf{I}_U$. By assuming that these symbols are drawn from a Gaussian distribution, (5.10) can be decomposed using Bussgang's theorem. Hence, by inserting the linear decomposition of (5.10) into (5.9), lower bounds on the sum rate achievable with Gaussian inputs can be found by following the procedure in Sec. 4.3.

More sophisticated nonlinear precoding schemes are known to outperform linear precoders at the cost of an increased computational complexity (see, e.g., [99,141–151]). The nonlinear precoders considered in this thesis seek optimal and suboptimal solutions to the MSE-optimal quantized precoding problem put forward in [99], which can be formulated as follows:

$$
\begin{aligned}
& \underset{\mathbf{x}^{\mathrm{dl}}[n]\in\mathcal{X}^B,\,\beta\in\mathbb{R}}{\text{minimize}} && \|\mathbf{s}^{\mathrm{dl}}[n] - \beta\mathbf{H}^T\mathbf{x}^{\mathrm{dl}}[n]\|_2^2 + \beta^2 U N_0^{\mathrm{dl}} \\
& \text{subject to} && \|\mathbf{x}^{\mathrm{dl}}[n]\|_2^2 \leq P^{\mathrm{ul}} \ \text{ and } \ \beta > 0.
\end{aligned}
\tag{5.11}
$$

For 1-bit DACs, for which it holds that $\mathcal{X} = \sqrt{P^{\mathrm{ul}}/2}\,\{1+j, -1+j, -1-j, \ 1-j\}$ and $\|\mathbf{x}^{\mathrm{dl}}[n]\|_2^2 = P^{\mathrm{ul}}$, this problem is solved exactly in [152] for small-to-moderate sized MU-MIMO systems via branch and bound. Unfortunately, the optimization problem (5.11) is, in general, NP-hard due to the nonconvex constraint $\mathbf{x}^{\mathrm{dl}}[n] \in \mathcal{X}^B$, which implies that exact solutions are not attainable for massive MU-MIMO systems. In this thesis, by relaxing the finite-alphabet constraint to a convex set, we shall develop efficient suboptimal precoders (with near-optimal performance) that find approximate solutions to the MSE-optimal quantized precoding problem (5.11) in polynomial time.

Contributions

This chapter summarizes the contributions of the included papers.

6.1 Paper A

In Paper A, we consider a narrowband massive MU-MIMO uplink system, which operates over a frequency-flat Rayleigh block-fading channel, for the case when the BS is equipped with low-resolution Nyquist-rate ADCs. Our focus is on the case where neither the transmitter nor the receiver have any *a priori* CSI, which implies that the fading realizations have to be learned at the BS through channel estimation based on coarsely quantized observations of received training symbols.

Using Bussgang's theorem, we propose a linear channel estimator that takes the distortion caused by the finite-resolution ADCs into account, derive the Bussgang gain matrix in (5.3) for multi-bit nonuniform quantizers, and derive closed-form approximations for the rate achievable with Gaussian signaling and conventional linear combining schemes (e.g., MRC and ZF). These closed-form approximations, which are derived under the assumption that the distortion caused by the low-resolution ADCs is spatially white, turn out to be accurate in the low-SNR regime and to overestimate the achievable rate in the high-SNR regime.

We further present an easy-to-evaluate approximation for the rate achievable with finite-cardinality inputs. By comparing this approximation with a numerically computed lower bound on the achievable rate, we confirm its accuracy for a large range of SNR values.

We show that high-order constellations can be supported and that high sum-rate throughputs can be achieved with low-complexity signal processing schemes (e.g., linear channel estimation and linear combining) in the massive MU-MIMO uplink for the case when low-resolution (e.g., 1-bit) ADCs are used at the BS. For the system configurations considered in Paper A, it is shown that 3–4 ADC bits are sufficient to close the gap to the infinite-resolution (no quantization) performance. This holds also for the case when the UEs are received at vastly different power levels due to, e.g., imperfect power control.

6.2 Paper B

In Paper B, we propose linear and nonlinear precoding algorithms for the narrowband MU-MIMO downlink for the case in which BS is equipped with low-resolution Nyquist-rate DACs and have perfect CSI.

Using Bussgang's theorem, we derive lower bounds and closed-form approximations for the rate achievable with low-resolution DACs and conventional linear precoders (e.g., MRT and ZF) over a Rayleigh-fading channel. We also derive closed-form approximations for the bit error rate (BER) achievable with QPSK signaling and linear precoding. Furthermore, we provide the Bussgang gain matrix in (5.4) for multi-bit uniform quantizers. Our results suggest that high information rates and low BERs are achievable despite the adverse impact of the finite-resolution DACs. In particular, we demonstrate that, with linear precoding at the BS, 3–4 DAC bits are sufficient to close the gap to the infinite-resolution performance for the considered system configurations.

For the 1-bit-DAC case, linear precoding is, however, far from optimal. We develop several nonlinear precoding algorithms by formulating the MSE-optimal quantized precoding problem in (5.11) and by relaxing it to a convex problem that can be solved in a computationally efficient manner. Specifically, we find three distinct approximate solutions to (5.11) using squared infinity-norm Douglas-Rachford splitting (SQUID), semi-definite relaxation, and sphere decoding. Through numerical simulations, we demonstrate the superiority of the proposed nonlinear precoders over conventional linear precoders for the narrowband massive MU-MIMO downlink.

6.3 Paper C

In Paper C, we solve the MSE-optimal quantized precoding problem in (5.11) exactly via branch and bound for small-to-moderate sized MU-MIMO systems equipped with 1-bit DACs. Specifically, we reformulate the original NP-hard problem as a tree-search problem and use a number of techniques that improve the pruning efficiency without sacrificing optimality. The proposed MSE-optimal precoding algorithm is shown to outperform the nonlinear precoders proposed in Paper B for small-to-moderate sized MU-MIMO

systems but at a significantly higher complexity, which prevents its use for massive MU-MIMO systems.

6.4 Paper D

In Paper D, we consider the downlink of a wideband massive MU-MIMO system with linear precoding and oversampling low-resolution DACs at the BS. We focus on the practically relevant scenario in which OFDM is used to communicate over frequency-selective channels. Specifically, we extend the analysis in Paper B to provide a lower bound on the information-theoretic sum rate achievable in the quantized massive MU-MIMO-OFDM downlink, which can be evaluated exactly for the case of 1-bit DACs.

For the case of multi-bit DACs, we develop an approximate, yet accurate, model for the distortion caused by the DACs. The proposed approximation, which is valid for uniform quantization, takes into account the inherent spatial and temporal correlation in the DAC distortion and can be used to evaluate the aforementioned sum-rate lower bound. We also derive a simpler approximation for the DAC distortion, which treats this distortion as white (i.e., uncorrelated in both the spatial and the temporal domains). We show that such a crude model is accurate for medium-to-high resolution DACs and when the OSR is not too high, but is not sufficient to accurately describe the distortion caused by low-resolution (e.g., 1 bit) DACs. Hence, our results highlight the importance of taking into account the spatial and temporal correlation in the distortion caused by low-resolution DACs.

6.5 Paper E

In Paper E, by leveraging the results in Paper D, we analyze OOB emissions caused by oversampling low-resolution DACs in the massive MU-MIMO-OFM downlink. In this work, we consider a more realistic DAC model for which the reconstruction stage in Fig. 3.8 is not an ideal low-pass filter. Specifically, we consider a reconstruction stage that cascades a ZOH filter followed by a Butterworth low-pass filter.

We show that the transmit-power reduction enabled by the antenna array at the BS yields also a significant reduction of OOB emissions. However, due to the inherent spatial correlation in the distortion caused by low-resolution DACs, OOB emissions are beamformed, to some extent, in the direction of the desired in-band signal. This implies that OOB emissions can be significant in certain spatial directions even for very large antenna arrays. Finally, we show that there is a trade-off between SINDR, adjacent channel leakage ratio (ACLR), and PAPR. Indeed, improving the ACLR by using sharper analog filters to attenuate the severe OOB emissions caused by the low-resolution DACs results in a reduced SINDR and an increased PAPR. Our results show that by carefully tuning the parameters of the analog filters, one can achieve a significant reduction in OOB emissions with only a moderate degradation in BER performance.

6.6 Paper F

In Paper F, we consider nonlinear precoding for the massive MU-MIMO-OFDM downlink for the case of oversampling 1-bit DACs and frequency-selective channels. Specifically, we extend the SQUID algorithm put forward in Paper B to the case of OFDM signaling. We demonstrate through numerical simulations that the proposed SQUID-OFDM precoding algorithm outperforms conventional linear precoders in terms of BER. Finally, we investigate the computational complexity of SQUID-OFDM precoding and show that it scales linearly with the number of BS-side antenna elements.

6.7 Paper G

In Paper G, we study the impact on performance of hardware impairments in the frequency-selective massive MU-MIMO-OFDM uplink. Starting from behavioral models of nonideal hardware components, we leverage Bussgang's theorem to develop an accurate composite model for the distortion caused by nonlinear LNAs, LOs with phase noise, and oversampling finite-resolution ADCs. The proposed aggregate hardware-impairment model, which captures the inherent spatial and temporal correlation of the induced signal distortion, depends only on the second-order statistics of the received signal and on the parameters of the behavioral hardware models.

Bibliography

[1] Ericsson, "Ericsson mobility report," White Paper, Jun. 2019.

[2] A. Zaidi, F. Athley, J. Medbo, U. Gustavsson, G. Durisi, and X. Chen, *5G Physical Layer: Principles, Models and Technology Components.* Academic Press, 2018.

[3] M. Simsek, A. Aijaz, M. Dohler, J. Sachs, and G. Fettweis, "5G-enabled tactile internet," *IEEE J. Sel. Areas Commun.*, vol. 34, no. 3, pp. 460–473, Mar. 2016.

[4] Ericsson, "5G systems," White Paper, Jan. 2017.

[5] E. Dahlman, S. Parkvall, and J. Sköld, *5G NR; The Next Generation Wireless Access Technology.* Academic Press, 2018.

[6] S. Parkvall, E. Dahlman, A. Furuskär, and M. Frenne, "NR: The new 5G radio access technology," *IEEE Commun. Standards Mag.*, vol. 1, no. 4, pp. 24–30, Dec. 2017.

[7] G. Durisi, T. Koch, and P. Popovski, "Toward massive, ultrareliable, and low-latency wireless communication with short packets," *Proc. IEEE*, vol. 104, no. 9, pp. 1711–1725, Sep. 2016.

[8] C. Bockelmann, N. Pratas, H. Nikopour, K. Au, T. Svensson, C. Stefanovic, P. Popovski, and A. Dekorsy, "Massive machine-type communications in 5G: Physical and MAC-layer solutions," *IEEE Commun. Mag.*, vol. 54, no. 9, pp. 59–65, Sep. 2016.

[9] P. Schulz, M. Matthé, H. Klessig, and M. Simsek, "Latency critical IoT applications in 5G: Perspective on the design of radio interface and network architecture," *IEEE Commun. Mag.*, vol. 55, no. 2, pp. 70–78, Feb. 2017.

[10] Cisco, "Cisco visual networking index: Global mobile data traffic forecast update, 2017–2022," White Paper, Feb. 2019.

[11] A. Osseiran, F. Boccardi, V. Braun, K. Kasume, P. Marsch, M. Maternia, O. Queseth, M. Schellmann, H. Schotten, H. Taoka, H. Tullberg, M. A. Uusitalo, B. Timus, and M. Fallgren, "Scenarios for 5G mobile and wireless communications: The vision of the METIS project," *IEEE Commun. Mag.*, vol. 52, no. 5, pp. 26–35, May 2014.

[12] J. G. Andrews, S. Buzzi, W. Choi, S. V. Hanly, A. Lozano, A. C. K. Soong, and J. C. Zhang, "What will 5G be?" *IEEE J. Sel. Areas Commun.*, vol. 32, no. 6, pp. 1065–1082, Jun. 2014.

[13] F. Boccardi, R. W. Heath Jr., A. Lozano, T. L. Marzetta, and P. Popovski, "Five disruptive technology directions for 5G," *IEEE Commun. Mag.*, vol. 52, no. 2, pp. 74–80, Feb. 2014.

[14] J. Lee, E. Tejedor, K. Ranta-aho, H. Wang, K.-T. Lee, E. Semaan, E. Mohyeldin, J. Song, C. Bergljung, and S. Jung, "Spectrum for 5G: Global status, challenges, and enabling technologies," *IEEE Commun. Mag.*, vol. 56, no. 3, pp. 12–18, Mar. 2018.

[15] T. S. Rappaport, S. Sun, R. Mayzus, H. Zhao, Y. Azar, K. Wang, G. N. Wong, J. K. Schulz, M. Samimi, and F. Gutierrez, "Millimeter wave mobile communications for 5G cellular: It will work!" *IEEE Access*, vol. 1, pp. 335–349, May 2013.

[16] Z. Pi and F. Khan, "An introduction to millimeter-wave mobile broadband systems," *IEEE Commun. Mag.*, vol. 49, no. 6, pp. 101–107, Jun. 2011.

[17] X. Yang, M. Matthaiou, C.-K. Wen, and Jin, "Hardware-constrained millimeter-wave systems for 5G: Challenges, opportunities, and solutions," *IEEE Commun. Mag.*, vol. 57, no. 1, pp. 44–50, Jan. 2019.

[18] C. Jeon, "Data detection in massive MU-MIMO systems," Ph.D. dissertation, Cornell University, Ithaca, NY, USA, May 2019.

[19] E. Dahlman, S. Parkvall, and J. Sköld, *4G: LTE/LTE-Advanced for Mobile Broadband*. Academic Press, 2011.

[20] F. Boccardi, B. Clerckx, A. Ghosh, E. Hardouin, K. Kusume, E. Onggosanusi, and Y. Tang, "Multiple-antenna techniques in LTE-advanced," *IEEE Commun. Mag.*, vol. 50, no. 3, pp. 114–121, Mar. 2012.

[21] E. Perahia, "IEEE 802.11n development: History, process, and technology," *IEEE Commun. Mag.*, vol. 46, no. 7, pp. 48–55, Jul. 2008.

[22] B. Bellalta, "IEEE 802.11ax: High-efficiency WLANs," *IEEE Wireless Commun.*, vol. 23, no. 1, pp. 38–46, Feb. 2016.

[23] S. Cherry, "Edholm's law of bandwidth," *IEEE Spectr.*, vol. 41, no. 7, pp. 58–60, Jul. 2004.

[24] T. L. Marzetta, "Noncooperative cellular wireless with unlimited numbers of base station antennas," *IEEE Trans. Wireless Commun.*, vol. 9, no. 11, pp. 3590–3600, Nov. 2010.

[25] F. Rusek, D. Persson, B. Kiong, E. G. Larsson, T. L. Marzetta, O. Edfors, and F. Tufvesson, "Scaling up MIMO: Opportunities and challenges with very large large arrays," *IEEE Signal Process. Mag.*, vol. 30, no. 1, pp. 40–60, Jan. 2013.

[26] E. G. Larsson, F. Tufvesson, O. Edfors, and T. L. Marzetta, "Massive MIMO for next generation wireless systems," *IEEE Commun. Mag.*, vol. 52, no. 2, pp. 186–195, Feb. 2014.

[27] H. Q. Ngo, "Massive MIMO: Fundamentals and system designs," Ph.D. dissertation, Linköping University, Linköping, Sweden, 2015.

[28] T. L. Marzetta, E. G. Larsson, H. Yang, and H. Q. Ngo, *Fundamentals of Massive MIMO*. Cambridge Univ. Press, 2016.

[29] G. Fodor, N. Rajatheva, W. Zirwas, L. Thiele, M. Kurras, K. Guo, A. Tölli, J. H. Sørensen, and E. de Carvalho, "An overview of massive MIMO technology components in METIS," *IEEE Commun. Mag.*, vol. 55, no. 6, pp. 155–161, Jun. 2017.

[30] A. L. Swindlehurst, E. Ayanoglu, P. Heydari, and F. Capolino, "Millimeter-wave massive MIMO: The next wireless revolution?" *IEEE Commun. Mag.*, vol. 52, no. 9, pp. 56–62, Sep. 2014.

[31] U. Gustavsson, C. Sanchéz-Perez, T. Eriksson, F. Athley, G. Durisi, P. Landin, K. Hausmair, C. Fager, and L. Svensson, "On the impact of hardware impairments on massive MIMO," in *Proc. IEEE Global Telecommun. Conf. (GLOBECOM)*, Austin, TX, USA, Dec. 2014, pp. 294–300.

[32] E. Björnson, J. Hoydis, M. Kountouris, and M. Debbah, "Massive MIMO systems with non-ideal hardware: Energy efficiency, estimation, and capacity limits," *IEEE Trans. Inf. Theory*, vol. 11, no. 60, pp. 7112–7139, Nov. 2014.

[33] E. Björnson, M. Matthaiou, and M. Debbah, "Massive MIMO with non-ideal arbitrary arrays: Hardware scaling laws and circuit-aware design," *IEEE Trans. Wireless Commun.*, vol. 14, no. 8, pp. 4353–4368, Apr. 2015.

[34] C. Mollén, "High-end performance with low-end hardware: Analysis of massive MIMO base station transceivers," Ph.D. dissertation, Linköping University, Linköping, Sweden, 2018.

[35] L. Van der Perre, L. Liu, and E. G. Larsson, "Efficient DSP and circuit architectures for massive MIMO: State of the art and future directions," *IEEE Trans. Signal Process.*, vol. 66, no. 18, pp. 4717–4736, Sep. 2018.

[36] S. Jacobsson, U. Gustavsson, G. Durisi, and C. Studer, "Massive MU-MIMO-OFDM uplink with hardware impairments: Modeling and analysis," in *Proc. Asilomar Conf. Signals, Syst., Comput.*, Pacific Grove, CA, USA, Oct. 2018, pp. 1829–1835.

[37] D. M. Pozar, *Microwave and RF Design of Wireless Systems.* Wiley, 2000.

[38] B. Le, T. W. Rondeau, J. H. Reed, and C. W. Bostian, "Analog-to-digital converters," *IEEE Signal Process. Mag.*, vol. 22, no. 6, pp. 69–77, Nov. 2005.

[39] H.-S. Lee and C. G. Sodini, "Analog-to-digital converters: Digitizing the analog world," *Proc. IEEE*, vol. 96, no. 2, pp. 323–334, Feb. 2007.

[40] A. Alkhateeb, J. Mo, N. González Prelcic, and R. W. Heath Jr., "MIMO precoding and combining solutions for millimeter-wave systems," *IEEE Commun. Mag.*, vol. 52, no. 12, pp. 122–131, Dec. 2014.

[41] R. W. Heath Jr., N. González Prelcic, S. Rangan, W. Roh, and A. Sayeed, "An overview of signal processing techniques for millimeter wave MIMO systems," *IEEE J. Sel. Topics Signal Process.*, vol. 10, no. 3, pp. 436–453, Feb. 2016.

[42] K. Roth, H. Pirzadeh, A. L. Swindlehurst, and J. A. Nossek, "A comparison of hybrid beamforming and digital beamforming with low-resolution ADCs for multiple users and imperfect CSI," *IEEE J. Sel. Topics Signal Process.*, vol. 12, no. 3, pp. 484–498, Jun. 2018.

[43] A. F. Molisch, V. V. Ratnam, S. Han, Z. Li, S. L. H. Nguyen, L. Linsheng, and K. Haneda, "Hybrid beamforming for massive MIMO: A survey," *IEEE Commun. Mag.*, vol. 55, no. 9, pp. 134–141, Sep. 2017.

[44] J. Mo, A. Alkhateeb, S. Abu-Surra, and R. W. Heath Jr., "Hybrid architectures with few-bit ADC receivers: Achievable rates and energy-rate tradeoffs," *IEEE Trans. Wireless Commun.*, vol. 16, no. 4, pp. 2274–2287, Apr. 2017.

[45] W. B. Abbas, F. Gomez-Cuba, and M. Zorzi, "Millimeter wave receiver efficiency: A comprehensive comparison of beamforming schemes with low resolution ADCs," *IEEE Trans. Wireless Commun.*, vol. 16, no. 12, pp. 8131–8146, Dec. 2017.

[46] L. N. Ribeiro, S. Schwarz, M. Rupp, and A. L. F. de Almeida, "Energy efficiency of mmWave massive MIMO precoding with low-resolution DACs," *IEEE J. Sel. Topics Signal Process.*, vol. 12, no. 2, pp. 298–312, Apr. 2018.

[47] A. El Gamal and Y.-H. Kim, *Network Information Theory.* Cambridge Univ. Press, 2014.

[48] D. Tse and P. Viswanath, *Fundamentals of Wireless Communication.* Cambridge Univ. Press, 2005.

[49] H. Q. Ngo, E. G. Larsson, and T. L. Marzetta, "Energy and spectral efficiency of very large multiuser MIMO systems," *IEEE Trans. Commun.*, vol. 61, no. 4, pp. 1436 – 1449, April 2013.

[50] G. Caire and S. Shamai (Shitz), "On the achievable throughput of a multiantenna Gaussian broadcast channel," *IEEE Trans. Inf. Theory*, vol. 49, no. 7, pp. 1691–1706, Jul. 2003.

[51] W. Yu and J. M. Cioffi, "Sum capacity of Gaussian vector broadcast channels," *IEEE Trans. Inf. Theory*, vol. 50, no. 9, pp. 1875–1892, Sep. 2004.

[52] S. Viswanath, N. Jindal, and A. Goldsmith, "Duality, achievable rates, and sum-rate capacity of Gaussian MIMO broadcast channels," *IEEE Trans. Inf. Theory*, vol. 49, no. 10, pp. 2658–2668, Oct. 2003.

[53] P. Viswanath and D. Tse, "Sum capacity of the vector Gaussian broadcast channel and uplink–downlink duality," *IEEE Trans. Inf. Theory*, vol. 49, no. 8, pp. 1912–1921, Aug. 2003.

[54] M. H. Costa, "Writing on dirty paper," *IEEE Trans. Inf. Theory*, vol. 29, no. 3, pp. 439–441, May 1983.

[55] C. B. Peel, B. M. Hochwald, and A. L. Swindlehurst, "A vector-perturbation technique for near-capacity multiantenna multiuser communication—Part I: Channel inversion and regularization," *IEEE Trans. Commun.*, vol. 53, no. 1, pp. 195–202, Jan. 2005.

[56] R. D. Wesel and J. M. Cioffi, "Achievable rates for Tomlinson-Harashima precoding," *IEEE Trans. Inf. Theory*, vol. 44, no. 2, pp. 824–831, Mar. 1998.

[57] C. Windpassinger, R. F. H. Fischer, and J. B. Huber, "Lattice-reduction-aided broadcast precoding," *IEEE Trans. Commun.*, vol. 52, no. 12, pp. 2057–2060, Dec. 2004.

[58] B. M. Hochwald, C. B. Peel, and A. L. Swindlehurst, "A vector-perturbation technique for near-capacity multiantenna multiuser communication—Part II: Perturbation," *IEEE Trans. Commun.*, vol. 53, no. 3, pp. 537–544, Mar. 2005.

[59] H. Q. Ngo, E. G. Larsson, and T. L. Marzetta, "Massive MU-MIMO downlink TDD systems with linear precoding and downlink pilots," in *Proc. Allerton Conf. Commun., Contr., Comput.*, Monticello, IL, USA, Oct. 2013.

[60] S. M. Kay, *Fundamentals of Statistical Signal Processing, Volume I: Estimation Theory.* Prentice Hall, 1993.

[61] D. Hui and D. L. Neuhoff, "Asymptotic analysis of optimal fixed-rate uniform scalar quantization," *IEEE Trans. Inf. Theory*, vol. 47, no. 3, pp. 957–977, Mar. 2001.

[62] N. Al-Dhahir and J. M. Cioffi, "On the uniform ADC bit precision and clip level computation for a Gaussian signal," *IEEE Trans. Signal Process.*, vol. 44, no. 2, pp. 434–438, Feb. 1996.

[63] J. Max, "Quantizing for minimum distortion," *IRE Trans. Inf. Theory*, vol. 6, no. 1, pp. 7–12, Mar. 1960.

[64] S. P. Lloyd, "Least squares quantization in PCM," *IEEE Trans. Inf. Theory*, vol. 28, no. 2, pp. 129–137, Mar. 1982.

[65] F. Maloberti, *Data converters.* Springer, 2007.

[66] W. R. Bennett, "Spectra of quantized signals," *Bell Syst. Tech. J.*, vol. 27, no. 3, pp. 446–472, Jul. 1948.

[67] A. Gersho, "Principles of quantization," *IEEE Trans. Circuits Syst.*, vol. 25, no. 7, pp. 427–436, Jul. 1978.

[68] S. P. Lipshitz, R. A. Wannamaker, and J. Vanderkooy, "Quantization and dither: A theoretical survey," *J. Audio Eng. Soc.*, vol. 40, no. 5, pp. 355–375, May 1992.

[69] D. Marco and D. L. Neuhoff, "The validity of the additive noise model for uniform scalar quantizers," *IEEE Trans. Inf. Theory*, vol. 51, no. 5, pp. 1739–1755, May 2005.

[70] A. V. Oppenheim, R. W. Schafer, and J. R. Buck, *Discrete-Time Signal Processing.* Prentice Hall, 1998.

[71] B. Widrow and I. Kollár, *Quantization Noise: Roundoff Error in Digital Computation, Signal Processing, Control, and Communications.* Cambridge Univ. Press, 2008.

[72] T. S. Rappaport, R. W. Heath Jr., R. C. Daniels, and J. N. Murdock, *Millimeter Wave Wireless Communications.* Prentice Hall, 2015.

[73] R. H. Walden, "Analog-to-digital converter survey and analysis," *IEEE J. Sel. Areas Commun.*, vol. 17, no. 4, pp. 539–550, Apr. 1999.

[74] B. Murmann, "A/D converter trends: Power dissipation, scaling and digitally assisted architectures," in *Proc. IEEE Custom Integrated Circuits Conf. (CICC)*, San Jose, CA, USA, Sep. 2008, pp. 105–112.

[75] R. Schreier and G. C. Temes, *Understanding Delta-Sigma Data Converters.* Wiley-IEEE Press, 2004.

[76] A. M. A. Ali, A. Morgan, C. Dillon, G. Patterson, S. Pucket, P. Bhoraskar, H. Dinc, M. Hensley, R. Stop, S. Bardsley, D. Lattimore, J. Bray, C. Speir, and R. Sneed, "A 16-bit 250-ms/s IF sampling pipelined ADC with background calibration," *IEEE J. Solid-State Circuits*, vol. 45, no. 12, pp. 2602–2612, Dec. 2010.

[77] B. Murmann, "ADC performance survey 1997-2019." [Online]. Available: http://web.stanford.edu/~murmann/adcsurvey.html

[78] Texas Instruments, "ADC31JB68 single-channel, 16-bit, 500-MSPS analog-to-digital converter," Data Sheet, Jan. 2019.

[79] ——, "DAC31x1 single-channel, 14-, 12-, and 10-bit, 500-MSPS, digital-to-analog converters," Data Sheet, Feb. 2018.

[80] W.-H. Tseng, C.-W. Fan, and J.-T. Wu, "A 12-bit 1.25-GS/s DAC in 90 nm CMOS with > 70 dB SFDR up to 500 MHz," *IEEE J. Solid-State Circuits*, vol. 46, no. 12, pp. 2845–2855, Dec. 2011.

[81] W.-T. Lin, H.-Y. Huang, and T.-H. Kuo, "A 12-bit 40 nm DAC achieving SFDR > 70 dB at 1.6 GS/s and IMD < −61 dB at 2.8 GS/s with DEMDRZ technique," *IEEE J. Solid-State Circuits*, vol. 49, no. 3, pp. 708–717, Mar. 2014.

[82] M. Liu, Z. Zhu, and Y. Yang, "A high-SFDR 14-bit 500 MS/s current-steering D/A converter in 0.18 μm CMOS," *IEEE Trans. VLSI Syst.*, vol. 23, no. 12, pp. 3148–3152, Dec. 2015.

[83] J. J. Bussgang, "Crosscorrelation functions of amplitude-distorted Gaussian signals," Res. Lab. Elec., Cambridge, MA, USA, Tech. Rep. 216, Mar. 1952.

[84] G. Jacovitti, A. Neri, and R. Cusani, "Methods for estimating the autocorrelation function of complex Gaussian stationary processes," *IEEE Trans. Acoust., Speech, Signal Process.*, vol. 35, no. 8, pp. 1126–1138, Aug. 1987.

[85] N. Y. Ermolova and S.-G. Häggman, "An extension of Bussgang's theory to complex-valued signals," in *Norwegian Sig. Process. Symp. (NORSIP)*, Espoo, Finland, Jun. 2004, pp. 45–48.

[86] H. E. Rowe, "Memoryless nonlinearities with Gaussian inputs: Elementary results," *Bell Labs Tech. J.*, vol. 61, no. 7, pp. 1519–1525, Sep. 1982.

[87] D. Dardari, V. Tralli, and A. Vaccari, "A theoretical characterization of nonlinear distortion effects in OFDM systems," *IEEE Trans. Commun.*, vol. 48, no. 10, pp. 1755–1764, Oct. 2000.

[88] W. Zhang, "A general framework for transmission with transceiver distortion and some applications," *IEEE Trans. Commun.*, vol. 60, no. 2, pp. 384–399, Feb. 2012.

[89] S. Dimitrov, S. Sinanovic, and H. Haas, "Clipping noise in OFDM-based optical wireless communication systems," *IEEE Trans. Commun.*, vol. 60, no. 4, pp. 1072–1081, Apr. 2012.

[90] P. Händel and D. Rönnow, "Dirty MIMO transmitters: Does it matter?" *IEEE Trans. Wireless Commun.*, vol. 17, no. 8, pp. 5425–5436, Aug. 2018.

[91] N. N. Moghadam, G. Fodor, M. Bengtsson, and D. J. Love, "On the energy efficiency of MIMO hybrid beamforming for millimeter-wave systems with nonlinear power amplifiers," *IEEE Trans. Wireless Commun.*, vol. 17, no. 11, pp. 7208–7221, Nov. 2018.

[92] E. Björnson, L. Sanguinetti, and J. Hoydis, "Hardware distortion correlation has negligible impact on UL massive MIMO spectral efficiency," *IEEE Trans. Commun.*, vol. 67, no. 2, pp. 1085–1098, Feb. 2019, to appear.

[93] O. De Candido, H. Jedda, A. Mezghani, A. L. Swindlehurst, and J. A. Nossek, "Reconsidering linear transmit signal processing in 1-bit quantized multi-user MISO systems," *IEEE Trans. Wireless Commun.*, vol. 18, no. 1, pp. 254–267, Jan. 2019.

[94] S. Rezaei Aghdam, S. Jacobsson, and T. Eriksson, "Distortion-aware linear precoding for millimeter-wave multiuser MISO downlink," in *Proc. IEEE Int. Conf. Commun. Workshop (ICCW)*, Shanghai, China, May 2019, to appear.

[95] A. S. Lan, M. Chiang, and C. Studer, "Linearized binary regression," in *Conf. Inf. Sciences Syst. (CISS)*, Princeton, NJ, USA, Mar. 2018.

[96] R. Ghods, A. S. Lan, T. Goldstein, and C. Studer, "Phaselin: Linear phase retrieval," in *Conf. Inf. Sciences Syst. (CISS)*, Princeton, NJ, USA, Mar. 2018.

[97] F. Wendler, M. Stein, A. Mezghani, and J. A. Nossek, "Quantization-loss reduction for 1-bit BOC positioning," in *ION Int. Tech. Meeting*, San Diego, CA, USA, Jan. 2013.

[98] T. Koch and A. Lapidoth, "At low SNR, asymmetric quantizers are better," *IEEE Trans. Inf. Theory*, vol. 59, no. 9, pp. 5421–5445, Sep. 2013.

[99] S. Jacobsson, G. Durisi, M. Coldrey, T. Goldstein, and C. Studer, "Quantized precoding for massive MU-MIMO," *IEEE Trans. Commun.*, vol. 65, no. 11, pp. 4670–4684, Nov. 2017.

[100] S. Jacobsson, G. Durisi, M. Coldrey, U. Gustavsson, and C. Studer, "Throughput analysis of massive MIMO uplink with low-resolution ADCs," *IEEE Trans. Wireless Commun.*, vol. 16, no. 6, pp. 4038–4051, Jun. 2017.

[101] D. M. Arnold, H.-A. Loeliger, P. O. Vontobel, A. Kavcic, and W. Zeng, "Simulation-based computation of information rates for channels with memory," *IEEE Trans. Inf. Theory*, vol. 52, no. 8, pp. 3498–3508, Aug. 2006.

[102] T. M. Cover and J. A. Thomas, *Elements of Information Theory*.   Wiley, 2006.

[103] A. Lapidoth, "Mismatched decoding and the multiple access channel," *IEEE Trans. Inf. Theory*, vol. 42, no. 5, pp. 1439–1452, Sep. 1996.

[104] J. Singh, O. Dabeer, and U. Madhow, "On the limits of communication with low-precision analog-to-digital conversion at the receiver," *IEEE Trans. Commun.*, vol. 57, no. 12, pp. 3629–3639, Dec. 2009.

[105] A. J. Viterbi and J. K. Omura, *Principles of Digital Communication and Coding*. McGraw-Hill, 1979.

[106] S. Jacobsson, M. Coldrey, G. Durisi, and C. Studer, "On out-of-band emissions of quantized precoding in massive MU-MIMO-OFDM," in *Proc. Asilomar Conf. Signals, Syst., Comput.*, Pacific Grove, CA, USA, Oct.–Nov. 2017, pp. 21–26.

[107] C. Mollén, E. G. Larsson, and T. Eriksson, "Waveforms for the massive MIMO downlink: Amplifier efficiency, distortion, and performance," *IEEE Trans. Commun.*, vol. 64, no. 12, pp. 5050–5063, Dec. 2016.

[108] K. Li, R. R. Sharan, Y. Chen, T. Goldstein, J. R. Cavallaro, and C. Studer, "Decentralized baseband processing for massive MU-MIMO systems," *IEEE J. Emerging Sel. Topics Circuits Syst.*, vol. 7, no. 4, pp. 491–507, Dec. 2017.

[109] S. Jacobsson, G. Durisi, M. Coldrey, and C. Studer, "Linear precoding with low-resolution DACs for massive MU-MIMO-OFDM downlink," *IEEE Trans. Wireless Commun.*, vol. 18, no. 3, pp. 1595–1609, Mar. 2019.

[110] H. Q. Ngo, A. Ashikhmin, H. Yang, E. G. Larsson, and T. L. Marzetta, "Cell-free massive MIMO versus small cells," *IEEE Trans. Wireless Commun.*, vol. 16, no. 3, pp. 1834–1850, Mar. 2017.

[111] S.-H. Park, O. Simeone, O. Sahin, and S. Shamai (Shitz), "Fronthaul compression for cloud radio access networks: Signal processing advances inspired by network information theory," *IEEE Signal Process. Mag.*, vol. 31, no. 6, pp. 69–79, Nov. 2014.

[112] M. Peng, C. Wang, V. Lau, and H. V. Poor, "Fronthaul-constrained cloud radio access networks: insights and challenges," *IEEE Wireless Commun.*, vol. 22, no. 2, pp. 152–160, Apr. 2015.

[113] Analog Devices, "JESD204B survival guide: Practical JESD204B technical information, tips, and advice from the world's data converter market share leader," Technical Paper, 2013.

[114] Ericsson AB, Huawei Technologies Co. Ltd, NEC Corporation, and Nokia, "Common public radio interface: eCPRI interface specification," eCPRI specification v1.0, Aug. 2017.

[115] A. Wadhwa and U. Madhow, "Blind phase/frequency synchronization with low-precision ADC: A Bayesian approach," in *Allerton Conf. Commun., Contr., Comput.*, Monticello, IL, USA, Oct. 2013.

[116] M. S. Stein, "Performance analysis for time-of-arrival estimation with oversampled low-complexity 1-bit A/D conversion," in *Proc. IEEE Int. Conf. Acoust., Speech, Signal Process. (ICASSP)*, New Orleans, LA, USA, Mar. 2017, pp. 4491–4495.

[117] S. Jacobsson, C. Lindquist, G. Durisi, T. Eriksson, and C. Studer, "Timing and frequency synchronization for 1-bit massive MU-MIMO-OFDM downlink," in *IEEE Int. Workshop Signal Process. Advances Wireless Commun. (SPAWC)*, Cannes, France, Jul. 2019, to appear.

[118] N. J. Myers and R. W. Heath Jr., "Message passing-based joint CFO and channel estimation in millimeter wave systems with one-bit ADCs," *IEEE Trans. Wireless Commun.*, vol. 18, no. 6, pp. 3064–3077, Jun. 2019.

[119] M. Schlüter, M. Dörpinghaus, and G. P. Fettweis, "On the timing synchronization under 1-bit quantization and oversampling," in *Proc. IEEE Workshop Stat. Signal Process. (SSP)*, Freiburg, Germany, Jun. 2018, pp. 198–202.

[120] S. Wang, Y. Li, and J. Wang, "Multiuser detection in massive spatial modulation MIMO with low-resolution ADCs," *IEEE Trans. Wireless Commun.*, vol. 14, no. 4, pp. 2156–2168, Apr. 2015.

[121] S. Jacobsson, G. Durisi, M. Coldrey, U. Gustavsson, and C. Studer, "One-bit massive MIMO: Channel estimation and high-order modulations," in *Proc. IEEE Int. Conf. Commun. Workshop (ICCW)*, London, U.K., Jun. 2015, pp. 1304–1309.

[122] O. Orhan, E. Erkip, and S. Rangan, "Low power analog-to-digital conversion in millimeter wave systems: Impact of resolution and bandwidth on performance," in *Proc. Inf. Theory Applicat. Workshop (ITA)*, San Diego, CA, USA, Feb. 2015, pp. 191–198.

[123] C.-K. Wen, C.-J. Wang, S. Jin, K.-K. Wong, and P. Ting, "Bayes-optimal joint channel-and-data estimation for massive MIMO with low-precision ADCs," *IEEE Trans. Signal Process.*, vol. 64, no. 10, pp. 2541–2556, Jul. 2015.

[124] C. Desset and L. V. d. Perre, "Validation of low-accuracy quantization in massive MIMO and constellation EVM analysis," in *Proc. Eur. Conf. Netw. Commun. (EuCNC)*, Paris, France, Jul. 2015, pp. 21–25.

[125] L. Fan, S. Jin, C.-K. Wen, and H. Zhang, "Uplink achievable rate for massive MIMO systems with low-resolution ADC," *IEEE Commun. Lett.*, vol. 19, no. 12, pp. 2186 – 2189, Dec. 2015.

[126] J. Zhang, L. Dai, S. Sun, and Z. Wang, "On the spectral efficiency of massive MIMO systems with low-resolution ADCs," *IEEE Commun. Lett.*, vol. 20, no. 5, pp. 842 – 845, Dec. 2015.

[127] J. Mo, P. Schniter, and R. W. Heath Jr., "Channel estimation in broadband millimeter wave MIMO systems with few-bit ADCs," *IEEE Trans. Signal Process.*, vol. 66, no. 5, pp. 1141–1154, Mar. 2016.

[128] J. Choi, J. Mo, and R. W. Heath Jr., "Near maximum-likelihood detector and channel estimator for uplink multiuser massive MIMO systems with one-bit ADCs," *IEEE Trans. Commun.*, vol. 64, no. 5, pp. 2005–2018, May 2016.

[129] N. Liang and W. Zhang, "Mixed-ADC massive MIMO," *IEEE J. Sel. Areas Commun.*, vol. 34, no. 4, pp. 983–997, May 2016.

[130] C. Studer and G. Durisi, "Quantized massive MU-MIMO-OFDM uplink," *IEEE Trans. Commun.*, vol. 64, no. 6, pp. 2387–2399, Jun. 2016.

[131] C. Mollén, J. Choi, E. G. Larsson, and R. W. Heath Jr., "Uplink performance of wideband massive MIMO with one-bit ADCs," *IEEE Trans. Wireless Commun.*, vol. 16, no. 1, pp. 87–100, Jan. 2017.

[132] Y. Li, C. Tao, G. Seco-Granados, A. Mezghani, A. L. Swindlehurst, and L. Liu, "Channel estimation and performance analysis of one-bit massive MIMO systems," *IEEE Trans. Signal Process.*, vol. 65, no. 15, pp. 4075–4089, Aug. 2017.

[133] M. Sarajalic, L. Liu, and O. Edfors, "When are low resolution ADCs energy efficient in massive MIMO?" *IEEE Access*, vol. 5, pp. 14 837–14 853, Nov. 2017.

[134] Y.-S. Jeon, N. Lee, S.-N. Hong, and R. W. Heath Jr., "One-bit sphere decoding for uplink massive mimo systems with one-bit ADCs," *IEEE Trans. Wireless Commun.*, vol. 17, no. 7, pp. 4509–4521, Jul. 2018.

[135] Y.-S. Jeon, S.-N. Hong, and N. Lee, "Supervised-learning-aided communication framework for massive MIMO systems with low-resolution ADCs," *IEEE Trans. Veh. Technol.*, vol. 67, no. 8, pp. 7299–7313, Aug. 2018.

[136] J. H. Van Vleck and D. Middleton, "The spectrum of clipped noise," *Proc. IEEE*, vol. 54, no. 1, pp. 2–19, Jan. 1966.

[137] B. Li, L. N., and W. Zhang, "On transmission model for massive MIMO under low-resolution output quantization," in *Proc. IEEE Veh. Technol. Conf. Spring (VTC-Spring)*, Sydney, NSW, Australia, Jun. 2017.

[138] A. Mezghani and J. A. Nossek, "Capacity lower bound of MIMO channels with output quantization and correlated noise," in *IEEE Int. Symp. Inf. Theory (ISIT)*, Cambridge, MA, USA, Jul. 2012.

[139] A. Mezghani, R. Ghiat, and J. A. Nossek, "Transmit processing with low resolution D/A-converters," in *Proc. IEEE Int. Conf. Electron., Circuits, Syst. (ICECS)*, Yasmine Hammamet, Tunisia, Dec. 2009, pp. 683–686.

[140] A. K. Saxena, I. Fijalkow, and A. L. Swindlehurst, "Analysis of one-bit quantized precoding for the multiuser massive MIMO downlink," *IEEE Trans. Signal Process.*, vol. 65, no. 17, pp. 4624–4634, Sep. 2017.

[141] O. Castañeda, S. Jacobsson, G. Durisi, M. Coldrey, T. Goldstein, and C. Studer, "1-bit massive MU-MIMO precoding in VLSI," *IEEE J. Emerging Sel. Topics Circuits Syst.*, vol. 7, no. 4, pp. 508–522, Dec. 2017.

[142] S. Jacobsson, G. Durisi, M. Coldrey, T. Goldstein, and C. Studer, "Nonlinear 1-bit precoding for massive MU-MIMO with higher-order modulation," in *Proc. Asilomar Conf. Signals, Syst., Comput.*, Pacific Grove, CA, USA, Nov. 2016, pp. 763–767.

[143] H. Jedda, A. Mezghani, A. L. Swindlehurst, and J. A. Nossek, "Quantized constant envelope precoding with PSK and QAM signaling," *IEEE Trans. Wireless Commun.*, vol. 17, no. 12, pp. 8022–8034, Oct. 2018.

[144] L. Landau and R. C. de Lamare, "Branch-and-bound precoding for multiuser MIMO systems with 1-bit quantization," *IEEE Wireless Commun. Lett.*, vol. 6, no. 6, pp. 770–773, Dec. 2017.

[145] A. Li, C. Masouros, F. Liu, and A. L. Swindlehurst, "Massive MIMO 1-bit DAC transmission: A low-complexity symbol scaling approach," *IEEE Trans. Wireless Commun.*, vol. 17, no. 11, pp. 7559–7575, Sep. 2018.

[146] A. Mezghani, R. Ghiat, and J. A. Nossek, "Tomlinson Harashima precoding for MIMO systems with low resolution D/A-converters," in *Int. ITG Workshop on Smart Antennas (WSA)*, Berlin, Germany, Feb. 2009.

[147] S. Jacobsson, O. Castañeda, C. Jeon, G. Durisi, and C. Studer, "Nonlinear precoding for phase-quantized constant-envelope massive MU-MIMO-OFDM," in *Proc. IEEE Int. Conf. Telecommunications (ICT)*, St. Malo, France, Jun. 2018, pp. 367–372.

[148] A. Nedelcu, F. Steiner, M. Staudacher, G. Kramer, W. Zirwas, R. Sisava Ganesan, P. Baracca, and S. Wesemann, "Quantized precoding for multi-antenna downlink channels with MAGIQ," in *Int. ITG Workshop on Smart Antennas (WSA)*, Bochum, Germany, Mar. 2017.

[149] M. Shao, Q. Li, and W.-K. Ma, "One-bit massive MIMO precoding via minimum symbol-error probability design," in *Proc. IEEE Int. Conf. Acoust., Speech, Signal Process. (ICASSP)*, Calgary, AB, Canada, Mar. 2018, pp. 3579–3583.

[150] F. Sohrabi, Y.-F. Liu, and W. Yu, "One-bit precoding and constellation range design for massive MIMO with QAM signaling," *IEEE J. Sel. Topics Signal Process.*, vol. 12, no. 3, pp. 557–570, Jun. 2018.

[151] C.-J. Wang, C.-K. Wen, S. Jin, and S.-H. Tsai, "Finite-alphabet precoding for massive MU-MIMO," *IEEE Trans. Wireless Commun.*, vol. 7, no. 7, pp. 4706–4720, May 2018.

[152] S. Jacobsson, W. Xu, G. Durisi, and C. Studer, "MSE-optimal 1-bit precoding for multiuser MIMO via branch and bound," in *Proc. IEEE Int. Conf. Acoust., Speech, Signal Process. (ICASSP)*, Calgary, AB, Canada, Apr. 2018, pp. 3589–3593.